Convective-Scale Structure and Evolution during a High-Resolution Simulation of Tropical Cyclone Rapid Intensification

ROBERT ROGERS

NOAA/AOML/Hurricane Research Division, Miami, Florida

ABSTRACT

The role of convective-scale processes in a 1.67-km mesoscale model simulation of the rapid intensification (RI) of Hurricane Dennis (2005) is presented. The structure and evolution of inner-core precipitating areas during RI, the statistical properties of precipitation during times experiencing vigorous convection (termed convective bursts here) and how they differ from nonburst times, possible differences in convective bursts associated with RI and those not associated with RI, and the impacts of precipitation morphology on the vortex-scale structure and evolution during RI are all examined. The onset of RI is linked to an increase in the areal extent of convective precipitation in the inner core, while the inner-core stratiform precipitating area remains unchanged and the intensity increases only after RI has begun. RI is not tied to a dramatic increase in the number of convective bursts nor in the characteristics of the bursts, such as burst intensity. Rather, the immediate cause of RI is a significant increase in updraft mass flux, particularly in the lowest 1.5 km. This increase in updraft mass flux is accomplished primarily by updrafts on the order of $1–2$ m s^{-1}, representing the bulk of the vertical motion distribution. However, a period of enhanced updraft mass flux in the midlevels by moderate to strong (>5 m s^{-1}) updrafts located inside the radius of maximum winds occurs $\sim$6 h prior to RI, indicating a synergistic relationship between convective bursts and the background secondary circulation prior to RI. This result supports the assertion that both buoyantly driven updrafts and slantwise near-neutral ascent are important features in eyewall structure, evolution, and intensification, including RI.

1. Introduction

One of the most challenging problems in tropical cyclone (TC) forecasting is predicting TC intensity change. While track forecasts have improved markedly in the past 20 years, progress in intensity forecasting has lagged significantly behind (Rogers et al. 2006; DeMaria et al. 2005). Intensity forecasting is challenging because the processes important in intensity change occur within and between scales of many orders of magnitude, including environmental, vortex, convective, turbulent, and microscales (Marks and Shay 1998). One subset of intensity change, rapid intensification (RI), is particularly difficult to predict. Typically defined as an increase of about 15 m s^{-1} in the maximum sustained surface wind speed in a 24-h period (Kaplan and DeMaria 2003), RI is significant from a forecasting perspective because of the

potential impacts of a storm that undergoes RI just prior to landfall.

Much of the research into intensity change and RI has focused on the environmental, vortex, and convective scales. Kaplan and DeMaria (2003), using the Statistical Hurricane Intensity Prediction Scheme (SHIPS) database, identified several environmental conditions associated with RI: warm sea surface temperatures and deep oceanic mixed layers, high lower-tropospheric relative humidity, low vertical shear, weak upper-level forcing from troughs or cold lows, and upper-level easterly flow. These findings are consistent with what has been found by previous observational and modeling studies on environmental conditions associated with intensity change and RI (e.g., Molinari et al. 1995; Bosart et al. 2000; Dunion and Velden 2004; Shay et al. 2000; Hong et al. 2000).

Processes that occur on the vortex scale have also been studied for their role in TC intensity change. From the axisymmetric perspective, it has long been known that intensity change to a large extent results from the cooperative interaction between the primary and secondary

Corresponding author address: Robert Rogers, NOAA/AOML/ Hurricane Research Division, 4301 Rickenbacker Cswy., Miami, FL 33149.
E-mail: robert.rogers@noaa.gov

circulations (e.g., Ooyama 1969, 1982; Schubert and Hack 1982), with the principal energy source arising from the extraction of latent energy from the ocean in the inflow and its subsequent release in the upward branch of the secondary circulation coinciding with the eyewall. Nolan and Grasso (2003) and Nolan et al. (2007) showed that it is the axisymmetric component of heating that dominates over asymmetric forcing in intensifying a TC. Other work has focused on the role of asymmetric processes in TC intensity change. Montgomery and Kallenbach (1997) showed that vortex Rossby waves intensify the axisymmetric primary circulation by axisymmetrizing convectively generated potential vorticity perturbations near the radius of maximum winds. Mesovortices are other asymmetric features that have been identified as being important for TC intensity change by mixing momentum, vorticity, and high-entropy air between the eye and eyewall (Schubert et al. 1999; Kossin and Schubert 2001; Montgomery et al. 2002; Persing and Montgomery 2003; Cram et al. 2007). Characteristics of the vortex favorable for intensification have been studied by Kossin and Eastin (2001), who found that the radial gradient of the angular velocity is an important determinant of a tropical cyclone's likelihood of intensification. They identified two regimes: one characterized by angular velocity that is greatest within the eyewall and relatively depressed within the eye (associated with intensifying TCs), and the other with radial profiles of angular velocity that are nearly monotonic, with maxima found at the eye center (peak intensity has been reached). Nolan et al. (2007) found that vortex amplification rates were also dependent on the strength, the vertical structure, and the latitude of the vortex.

Convective-scale processes have also been identified as being important in TC intensity change. Observational studies have linked intensity change, and RI in particular, to the intermittent occurrence of deep, strong convection (sometimes referred to as convective bursts) within the inner core (e.g., Reasor et al. 2009; Squires and Businger 2008; Hennon 2006; Kelley et al. 2004; Rodgers et al. 1998; Gentry et al. 1970). Convective bursts are recognized in many ways, with cloud tops getting colder and expanding in infrared (IR) measurements, very low brightness temperatures due to ice scattering in the passive microwave channels, an increase of lightning flash rates, and towers of high radar reflectivity (Cecil et al. 2002). The relationship between convective bursts and RI has generally been linked to enhanced latent heat release and subsidence in the storm core (e.g., Heymsfield et al. 2001), though some recent modeling studies have instead emphasized the importance of cyclonic rotation collocated with vigorous updrafts as being key (Montgomery et al. 2006; Hendricks et al. 2004).

These rotating updrafts, termed vortical hot towers (VHTs), were deemed vital in tropical cyclogenesis, and their importance has been extended to RI.

The role of diabatic heating associated with convective bursts in RI is likely dependent on the magnitude, duration, horizontal and vertical distributions, and the orientation of the heating relative to the radius of maximum winds (Schubert and Vigh 2008; Nolan et al. 2007). The morphology of the precipitation, for example, the distribution of convective precipitation and whether the precipitation is organized into a predominantly convective or stratiform mode, determines the horizontal and vertical structures and longevity of the diabatic heating, and may thus also play a significant role in determining the response of the vortex to the heating. Furthermore, the impacts of precipitation morphology on the vortex depend on the characteristics of the vortex itself, such as the strength of the primary and secondary circulations and the horizontal and vertical extents of the circulations (Pendergrass and Willoughby 2009; Shapiro and Willoughby 1982). Such characteristics determine the efficiency with which diabatic heating released within the storm core is converted into an increase in the kinetic energy of the storm (Pendergrass and Willoughby 2009; Nolan et al. 2007; Schubert and Hack 1982), manifested as a strengthening of the primary and secondary circulations and storm intensification.

While a general relationship between convective bursts and RI has been established, it is not clear whether bursts *cause* RI or are simply a reflection of other processes occurring within the vortex during RI. Malkus and Riehl (1960), Simpson et al. (1998), and Braun (2002, 2006) identified deep, undilute convective cores in the eyewall, which they termed hot towers, as accomplishing a significant portion of the vertical mass flux in the eyewall. These hot towers, termed convective bursts in the current parlance, are driven by local buoyancy, where ''local'' is meant to refer to their buoyancy relative to the immediate environment of the eyewall (Smith et al. 2005), and they play a key role in TC intensification in this theory. By contrast, Emanuel (1986) and Rotunno and Emanuel (1987) theorized that TC maintenance and intensification occurred in a state of near-symmetric neutrality, with the minimum central pressure determined by sea surface temperature (SST) and the temperature of the outflow layer. By this reasoning, it is a finite-amplitude air–sea interaction instability, and not penetrative convection caused by local buoyancy,[1] that is vital for TC intensification. In a study of flight-level observations

---

[1] Henceforth, unless otherwise noted, ''buoyancy'' will be considered as the local buoyancy, as in Smith et al. (2005).

from multiple storms, Eastin et al. (2005) found that eyewall vertical motion was a combination of both buoyantly driven updrafts and slantwise-neutral ascent. Buoyant convective updrafts, however, were integral components of the hurricanes' transverse circulation, so convective bursts likely play some role in RI.

The primary goal of this work is to address the importance of convective bursts in RI by examining the structure and evolution of convective-scale processes prior to and during RI. This examination will proceed via an evaluation of a cloud-resolving multiday simulation of Hurricane Dennis (2005), which underwent a period of RI beginning when it was still a tropical storm. Particular emphasis will be placed on examining the structure and evolution of inner-core convective variables, statistical properties of these variables during convective burst times and how they differ from nonburst times, possible differences in convective bursts associated with RI and those not associated with RI, and the impacts of precipitation morphology on the vortex-scale structure and evolution during RI.

2. Data and methodology

a. Case description

Hurricane Dennis developed from an easterly wave that entered the southeastern Caribbean Sea in early July 2005 (Beven 2008). Convection increased within a broad circulation, and a tropical depression was declared by the National Hurricane Center at 1800 UTC 4 July. From there the system moved to the west-northwest through the central Caribbean, steadily intensifying to a tropical storm by 1200 UTC 5 July (Fig. 1). Starting at 1800 UTC 6 July, the intensification rate of Tropical Storm Dennis increased, with the minimum sea level pressure dropping from 989 to 967 hPa and the peak 10-m winds increasing from 31 to 45 m s^{-1} in 18 h (the storm continued to intensify another 5 m s^{-1} during the following 6 h, for a total 24-h intensification of 19 m s^{-1} from 1800 UTC 6 July to 1800 UTC 7 July). Since the intensification rate increased at 1800 UTC 6 July, this time is considered the onset of RI for this study. The time period from just after tropical storm formation (i.e., 1800 UTC 5 July) to 1200 UTC 7 July, which includes the onset of RI, will be the focus of this work. The time from 1800 UTC 5 July to 1800 UTC 6 July is termed the pre-RI period, and the time from 1800 UTC 6 July to 1200 UTC 7 July is termed the RI period.

The large-scale environment during this time was generally favorable for storm intensification. Figure 2 shows 200- and 850-hPa fields at 0000 UTC 6 and 7 July from the 1° analyses from the National Centers for Environmental Prediction Global Forecasting System (GFS).

An anticyclone at 200 hPa is visible over the eastern Gulf of Mexico throughout this time, with weak easterly and northeasterly upper-level flow in the eastern Caribbean. At 850 hPa, there is a broad anticyclone in the western Atlantic and easterly flow associated with the easterly wave that became Dennis in the eastern Caribbean. Low-level relative humidity is high (>75%) in the vicinity of Dennis. Values of 850–200-hPa vertical shear magnitude diagnosed from SHIPS (not shown) are generally low, ranging from 2.5 m s^{-1} at 0000 UTC 6 July to 6.5 m s^{-1} at 0000 UTC 7 July. SST from SHIPS (not shown) ranges from 28.5° to 29°C during this time, and the area of the central Caribbean in which RI occurred climatologically has ocean mixed layer depths of 70–80 m, deeper than the adjacent waters of the western Atlantic.

Radar composites from the lower-fuselage (LF) radar on the National Oceanic and Atmospheric Administration (NOAA) P-3 aircraft that sampled the storm during 5–7 July (Fig. 3) show a broad shield of rainfall on the southeast side of the circulation center on 5 July, with some embedded cores of high reflectivity. During 6–7 July (Fig. 3b), the system has become much better organized, reaching hurricane status just prior to the radar sampling time. The radar pattern shows an eyewall with a diameter of about 40 km and a primary spiral rainband. The eyewall is open on the northwest side and high-reflectivity values are seen on the southeast side. Cores of high reflectivity continue to be seen both in the eyewall and within the spiral rainband.

b. Model description

The numerical model used is the fifth-generation Pennsylvania State University–National Center for Atmospheric Research Mesoscale Model (MM5; Grell et al. 1994). The MM5 is a fully nonlinear, nonhydrostatic mesoscale model that has a well-demonstrated ability to simulate tropical cyclones at cloud-resolving resolution (e.g., Liu et al. 1997; Karyampudi et al. 1998; Braun and Tao 2000; Braun 2002; Rogers et al. 2003, 2007). The model configuration used here is similar to previous studies (e.g., Rogers et al. 2003, 2007). A vortex-following nested grid is used that allows for long integrations with high resolution in the inner-core regions of hurricanes (Tenerelli and Chen 2004). Four domains are used, with grid lengths of 45, 15, 5, and 1.67 km. The innermost 1.67-km mesh contains 160 × 160 grid points in the horizontal for a total areal coverage of 267 km × 267 km, enough to include the inner core and most rainbands for the storm within this mesh. There are 36 vertical levels in the model, with vertical resolution maximized in the lowest 100 hPa (roughly 50-m spacing) and around the melting level (~550 hPa).
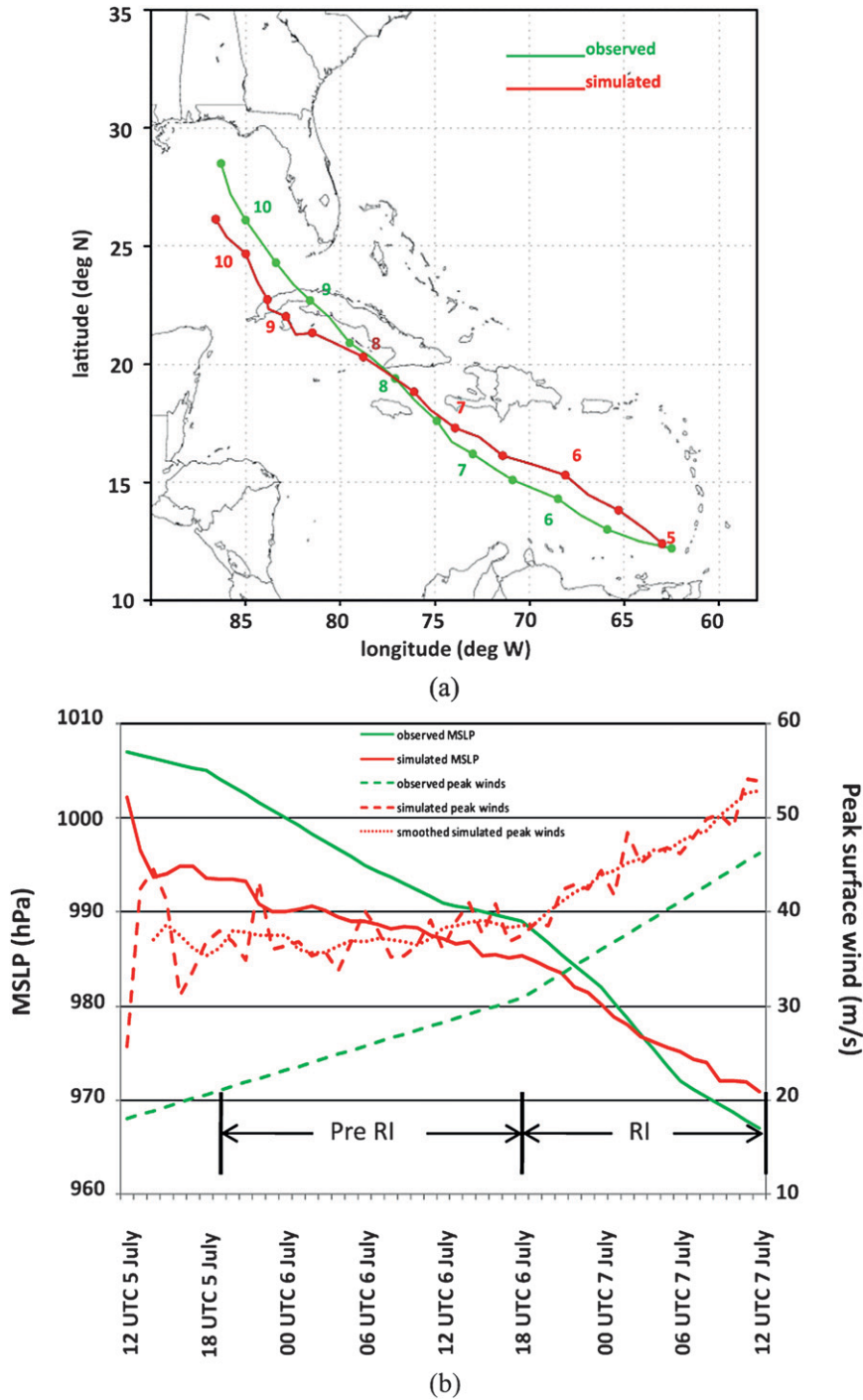
(a)

(b)

FIG. 1. (a) Plots of National Hurricane Center best-track position (green) and MM5-simulated position (red) of Hurricane Dennis at 12-h intervals from 0000 UTC 5 Jul to 1200 UTC Jul 10. (b) Plots of MSLP (solid) and peak surface winds (dashed) from 1200 UTC 5 Jul to 1200 UTC 7 Jul 2005. Best-track (simulated) values are shown as green (red) lines. Dotted red line in (b) shows the simulated intensity smoothed over a 5-h period. "Pre-RI" and "RI" time periods denoted in (b).
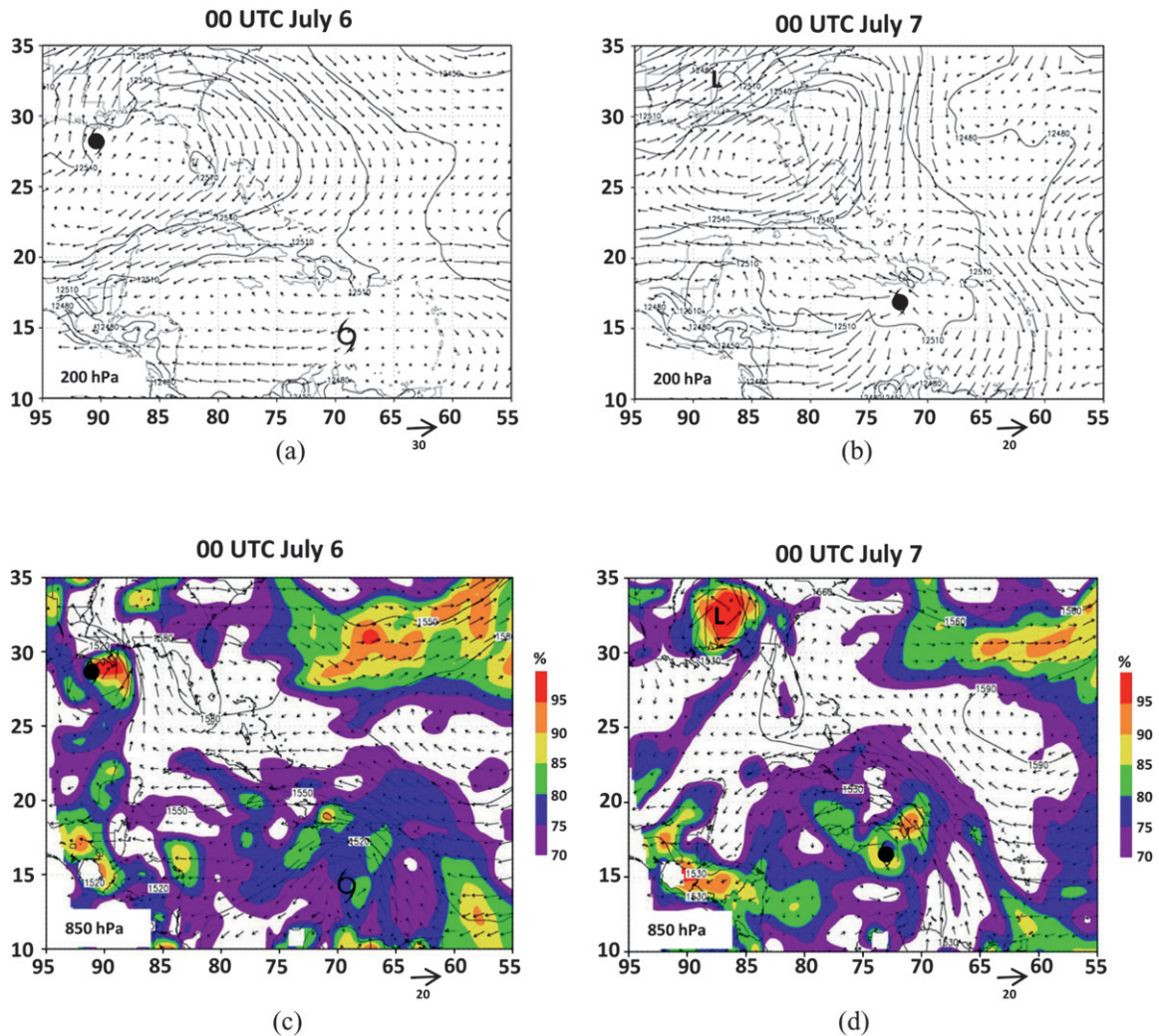
FIG. 2. GFS 1° analyses of (a) 200-hPa geopotential height (contours, m) and winds (vectors, m s^{-1}) at 0000 UTC 6 Jul and (b) 850-hPa geopotential height (contours, m), relative humidity (shaded, %), and winds (vectors, m s^{-1}) at 0000 UTC 6 Jul 2005. (c) As in (a) but at 0000 UTC 7 Jul. (d) As in (b) but at 0000 UTC 7 Jul. Locations of Cindy and Dennis in the analyses are denoted by hurricane, tropical storm, and tropical depression symbols.

The model initial and lateral boundary conditions for the outer-most domain during integration are from the GFS model 1° analysis fields. The 45-km mesh is initialized at 1200 UTC 4 July. The 15-km mesh is initialized 12 h later, and the 5- and 1.67-km meshes are initialized 12 h after that. In a manner similar to previous high-resolution simulations of tropical cyclones and tropical convection (Rogers et al. 2003, 2007; Chen et al. 2001), four-dimensional data assimilation (FDDA; Stauffer and Seaman 1990) is used to nudge the wind and temperature fields toward the analysis fields during the first 60 h of the simulation. This nudging, used only on the outer 45-km mesh, provides a better representation of the large-scale fields and, consequently, an improved storm track. It also provides improved boundary con-

ditions for the inner three meshes, which do not use any FDDA. Time-invariant sea surface temperatures use 9-km Advanced Very High Resolution Radiometer (AVHRR) Pathfinder SSTs into the SST field (Kilpatrick et al. 2001).

For the two outer meshes (45 and 15 km), the Kain–Fritsch convective parameterization scheme is used (Kain and Fritsch 1993). This scheme includes a relatively sophisticated cloud model that determines entrainment and detrainment rates as a function of the local environment and includes the effects of downdrafts. On the inner two meshes, the deepest and strongest convective towers are approximately resolved (especially for the 1.67-km mesh), so no convective parameterization scheme is used for those meshes. For the parameterization of vertical mixing, the Blackadar boundary layer parameterization

2130–2250 UTC 5 July

P-3 lower fuselage composite

(a)

0045–0145 UTC 7 July

P-3 lower fuselage composite

(b)

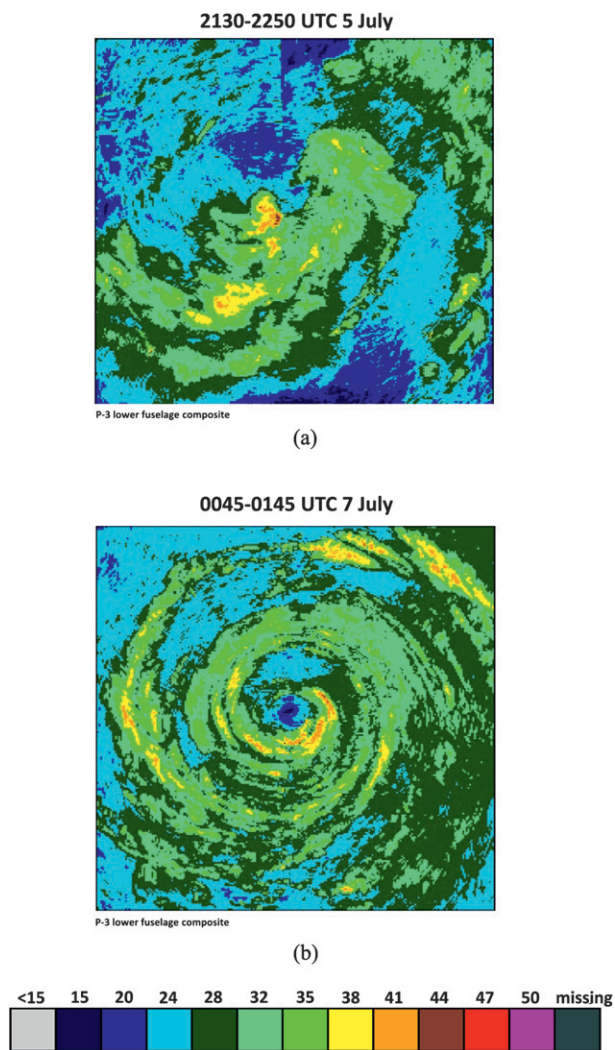| <15 | 15 | 20 | 24 | 28 | 32 | 35 | 38 | 41 | 44 | 47 | 50 | missing |

FIG. 3. NOAA P-3 LW radar reflectivity composites centered on the storm. (a) Composite at 3.6-km altitude from 2130 to 2249 UTC 5 Jul 2005. (b) Composite at 4.2-km altitude from 0045 to 0144 UTC 7 Jul. Domains shown are 240 km on a side.

scheme (Zhang and Anthes 1982) is used on all meshes. This scheme contains two different regimes of turbulent mixing to determine whether mixing is determined by local downgradient K theory (stable regime) or by the thermal stratification of the mixed layer and the surface heat flux (free convection regime). This PBL scheme configuration has been used to simulate Hurricane Bonnie of 1998 (Rogers et al. 2003), Hurricane Georges of 1998 (Cangialosi and Chen 2004), and Hurricane Floyd of 1999 (Tenerelli and Chen 2002). The fourth-order scheme of Smagorinsky et al. (1965) is used to parameterize horizontal diffusion. A simple radiation scheme that allows for the impacts of clouds on short-wave and longwave radiation is used (Dudhia 1989). The microphysical parameterization scheme used for all four

meshes is the Goddard scheme, which is a bulk single-moment three-class ice scheme that contains prognostic equations for cloud water (ice), rainwater (snow), and hail, and allows for the existence of supercooled water (Lin et al. 1983, Tao and Simpson 1989). The version of the Goddard scheme used here includes graupel instead of hail, as in Braun and Tao (2000). This scheme has been used in many tropical cyclone simulations, at grid lengths ranging from 1.3 to 81 km (e.g., Liu et al. 1997; Braun and Tao 2000; Davis and Bosart 2002; Rogers et al. 2007). This method includes condensation–evaporation, freezing–melting, sublimation–deposition, autoconversion (i.e., aggregation) of cloud water (ice, snow) to form rainwater (snow, hail/graupel), collection by rainwater (snow), and accretion.

c. Partitioning into convective and stratiform components

To facilitate an examination of the structure and evolution of precipitation within the TC inner core, the precipitating areas were partitioned into convective and stratiform components. The objective technique partitions precipitating areas primarily into two regimes that have long been recognized as being distinct, but important, components of mesoscale convective systems (MCSs; e.g., Houze 1977; Zipser 1977; Gamache and Houze 1982; Johnson 1984; Mapes and Houze 1995). Such a partitioning, representing a two-dimensional field, has generally been performed on MCSs embedded within a much less rotational environment than a TC. Precipitation partitioning in TCs from both observational and modeling studies (e.g., Black et al. 1996; Rogers et al. 2007) typically divide regions into eyewall, rainband, and stratiform areas. This division was not used here, though, because the partitioning is applied to a TC at an early stage in its life cycle, when the eyewall and rainbands are not yet developed. The use of a convective–stratiform partitioning technique in a mature hurricane may be limited due to strong tangential advection in the eyewall, but, as will be shown later, many of the primary features associated with convective and stratiform precipitation in MCSs are also seen using the partitioning algorithm discussed here.

The primary feature used in the convective–stratiform partitioning algorithm is the horizontal distribution of reflectivity, based on the algorithm in Steiner et al. (1995). The reflectivity criteria used to identify convective points relies on three factors: intensity of reflectivity, peakedness (excess of reflectivity over a background value), and all points within a prespecified distance, termed the convective radius, that surround a convective point. After that the remaining points are categorized as stratiform, other, and no rain, based on the reflectivity at 3-km altitude.

TABLE 1. Differences in the formulation of the convective–stratiform partitioning algorithm between Steiner et al. (1995) and the MM5 Dennis simulation shown here.

	MM5 simulation	Steiner et al. (1995) radar study
Altitudes checked (km)	0.9 and 3	3
Intensity threshold reflectivity (dBZ)	>46	>40
Peakedness reflectivity equation [Eq. (2) in Steiner et al. (1995)]	$\Delta Z = 15 - Z_{bg}^2/135$	$\Delta Z = 10 - Z_{bg}^2/180$
Threshold reflectivity for implementing Eq. (2) (dBZ)	>45	>42.43
Threshold vertical velocity check	>0.5 m s^{-1} over 0.9–2.1-km layer	None

The "other" category is applied at a grid point when the grid point is not classified as "convective" and the reflectivity at 3-km altitude is between 0 and 20 dBZ. Generally, the "other" category occurs near the edges of stratiform precipitation when there is high reflectivity aloft (>25 dBZ) but low reflectivity in the lower troposphere, which would be indicative of anvil-type precipitation. If the 3-km reflectivity is <0 dBZ and is not flagged as convective, the point is identified as "no rain." If the grid point is not convective and the 3-km reflectivity is >20 dBZ, it is flagged as stratiform. Threshold values for each of these criteria, originally developed for ground-based radar observations, were adapted to the simulated reflectivity fields, which have been known to show a pronounced high bias when compared to radar measurements (e.g., Rogers et al. 2007; Braun 2006; McFarquhar et al. 2006; Liu et al. 1997). To account for the sloping of convective features in the TC inner core (e.g., Marks 1985), two altitudes in the lower troposphere (0.9 and 3 km) and a threshold of vertical velocity averaged between 0.9 and 2.1 km are used to categorize points as being convective. A pass is made at the lower level to flag convective points, then another pass is made at the higher level to flag the remaining points as convective, and then the vertical velocity threshold is applied to flag the remaining points exceeding the threshold as convective. Steiner et al. (1995) provide a detailed description of these algorithms (e.g., peakedness criteria, convective radius formulation). Table 1 here provides key differences in the parameters used here and those used in Steiner et al.

3. Synoptic- and vortex-scale evolution

Hodographs of the environmental flow impacting the inner core of Dennis [calculated similarly to Rogers et al. (2003)] at 0000 UTC 6 and 7 July (Fig. 4a) show easterly and east-southeasterly flow between 850 and 200 hPa, with wind speeds throughout the layer remaining <10 m s^{-1} at both times. A time series of simulated 850–200-hPa shear magnitude and direction (Fig. 4b, calculated within a storm-centered 167-km box) shows that the shear magnitude remains northeasterly and <7.5 m s^{-1} for most of the simulation, including

during the onset of RI at 1800 UTC 6 July. This is generally consistent with the flow and shear fields seen in the global model and SHIPS analyses.

The simulated track of Dennis follows the best track very closely (Fig. 1). Simulated peak winds and minimum sea level pressure (MSLP) indicate that the simulated storm is stronger at the time the inner two meshes are
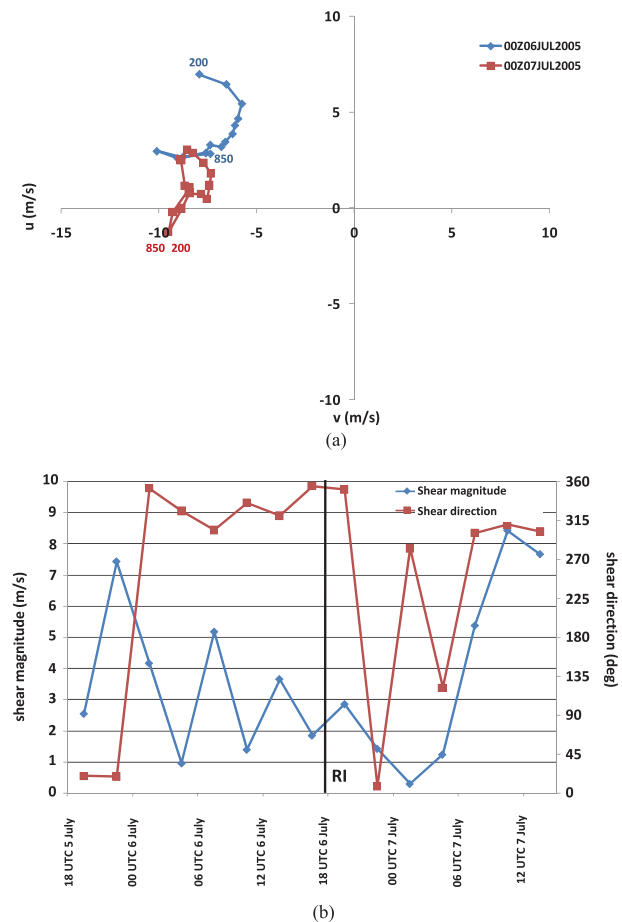

FIG. 4. (a) Hodographs from 850 to 200 hPa (m s^{-1}) in a 167-km box centered on storm at 0000 UTC 6 Jul (blue) and 0000 UTC 7 Jul (red) 2005. (b) Time series of 850–200-hPa shear magnitude (blue, m s^{-1}) and direction (red, °) in 10° box centered on the storm from 1800 UTC 5 Jul to 1200 UTC 7 Jul. Black line denotes the onset of RI.

initialized at 1200 UTC 5 July. At this time, there are some small oscillations in intensity during the first 6 h as the high-resolution meshes adjust to being initialized (see, e.g., Braun et al. 2006). Beginning at 1800 UTC 5 July, the storm steadily intensifies until 1800 UTC 6 July. At 1800 UTC 6 July, the intensification rate increases as the peak simulated winds increase from 37 to 54 m s^{-1} by 1200 UTC 7 July. This intensification rate (17 m s^{-1} in 18 h or about 20 m s^{-1} in a 24-h period) meets the requirement of RI according to the definition of Kaplan and DeMaria (2003). The onset of RI and the intensification rate during RI are nearly identical to the best track.

Plots of the simulated reflectivity at 850 hPa are shown in Fig. 5 for a period prior to and during RI. The horizontal distribution of the precipitation is broadly consistent with the LF reflectivity (cf. Fig. 3). At 1800 UTC 5 July, most of the precipitation is on the southeast side of the circulation with embedded cores of high reflectivity. During the next 24 h, the reflectivity field becomes better organized around the storm's center as the storm intensifies. Precipitation develops on the north and northwest sides of the circulation by 0600 UTC 6 July, and by 1800 UTC 6 July a closed eyewall has developed. Cores of high reflectivity, with maximum values exceeding 55 dBZ, occur within the eyewall and spiral rainband. The radius of peak reflectivity is about 50 km, which is larger than the observed radius of ~25 km (cf. Fig. 3). Early in the storm's evolution, the convective cores are more isolated, but as the storm intensifies the 40 + dBZ contour becomes elongated in the tangential direction. Similar to previous modeling studies, peak reflectivity values are higher in the simulation than the observations by 10–15 dBZ (e.g., Rogers et al. 2007).

Radius–height plots of azimuthally averaged winds and vorticity before and during RI are shown in Fig. 6. The height-varying vortex center was defined by the centroid of the potential vorticity. At 1200 UTC 6 July, the azimuthally averaged tangential wind ($\bar{u}_t$) shows a peak of 30 m s^{-1} at the top of the inflow layer 60 km from the center. The azimuthally averaged radial wind ($\bar{u}_r$) shows inflow of 6 m s^{-1} in the lowest 1 km and weak outflow above 12 km. Azimuthally averaged vertical relative vorticity ($\bar{\zeta}$, Fig. 6b) is maximized in the inner 20 km below 5-km altitude and decreases monotonically at larger radii. Azimuthally averaged vertical velocity ($\bar{w}$) shows a peak value of 0.8 m s^{-1} at 10-km altitude and 30-km radius, above the inner edge of the low-level inflow. During the next 12 h, RI begins, and both the primary and the secondary circulation patterns intensify markedly, with a broad area of tangential winds >35 m s^{-1} between 35- and 70-km radius and nearly 10 m s^{-1} inflow in the boundary layer at 0000 UTC

7 July. The radius of peak tangential winds has decreased from 60 to ~45 km, and the depth of the vortex has increased, with the vertical extent of the 25 m s^{-1} tangential wind contour increasing from 2-km altitude at 1200 UTC 6 July to nearly 8-km altitude at 0000 UTC 7 July. The slope of the eyewall, indicated by the angle between the axis of peak tangential wind (from Figs. 6a, 6c, and 6e) and the vertical, has also decreased, which is consistent with recent observational studies showing the eyewall slope decreasing with decreasing radius of maximum wind (Stern and Nolan 2009). The vorticity continues to show a maximum at the center of the storm, but now a secondary maximum is seen between 6- and 10-km altitude at 30-km radius, consistent with radial profiles of vorticity for intensifying TCs documented in flight-level data from Kossin and Eastin (2001). The $\bar{w}$ values reach a peak value of 1.4 m s^{-1} at 55-km radius at 5-km altitude, above the tangential wind peak.

Time–radius Hovmöller diagrams in Fig. 7 show the axisymmetric evolution of the storm. Figure 7a shows azimuthally averaged $\bar{u}_t$ and $\bar{u}_r$ at 0.3-km altitude from 1800 UTC 5 July to 1200 UTC 7 July. Initially, the vortex is weak, with peak tangential winds of 20 m s^{-1} broadly located between 30- and 60-km radius and radial inflow of 4–6 m s^{-1} farther outward. As time progresses, both $\bar{u}_t$ and $\bar{u}_r$ increase by 100%–200%, and after the onset of RI at 1800 UTC 6 July the peak in $\bar{u}_t$ contracts from 70- to 30-km radius. The plot of azimuthally averaged reflectivity at 3-km altitude and vertical motion averaged in the 0.3–1.5-km layer are both diffuse initially, but between 1200 and 1800 UTC 6 July a clear peak in reflectivity develops, coincident with eyewall formation (cf. Fig. 5), and contracts from 80- to 35-km radius by 1200 UTC 7 July. A band of enhanced low-level upward motion develops around 1800 UTC 6 July along the inner edge of the reflectivity peak and also contracts. Given this evolution, the region inside 75-km radius is considered to be a region distinct from that outside 75 km. The region inside 75 km is termed the inner core, as it contains the upward branch of the secondary circulation. The eyewall and a few inner rainbands are located within the inner core.

4. Convective-scale structure and evolution

As mentioned in the introduction, the role of the convective-scale structure and evolution in RI is largely determined by the temporal and spatial distributions of the diabatic heating. Important components of this relationship are the partitioning of the rainfall into convective and stratiform components, the possible role of convective bursts in governing RI, and the vortex-scale
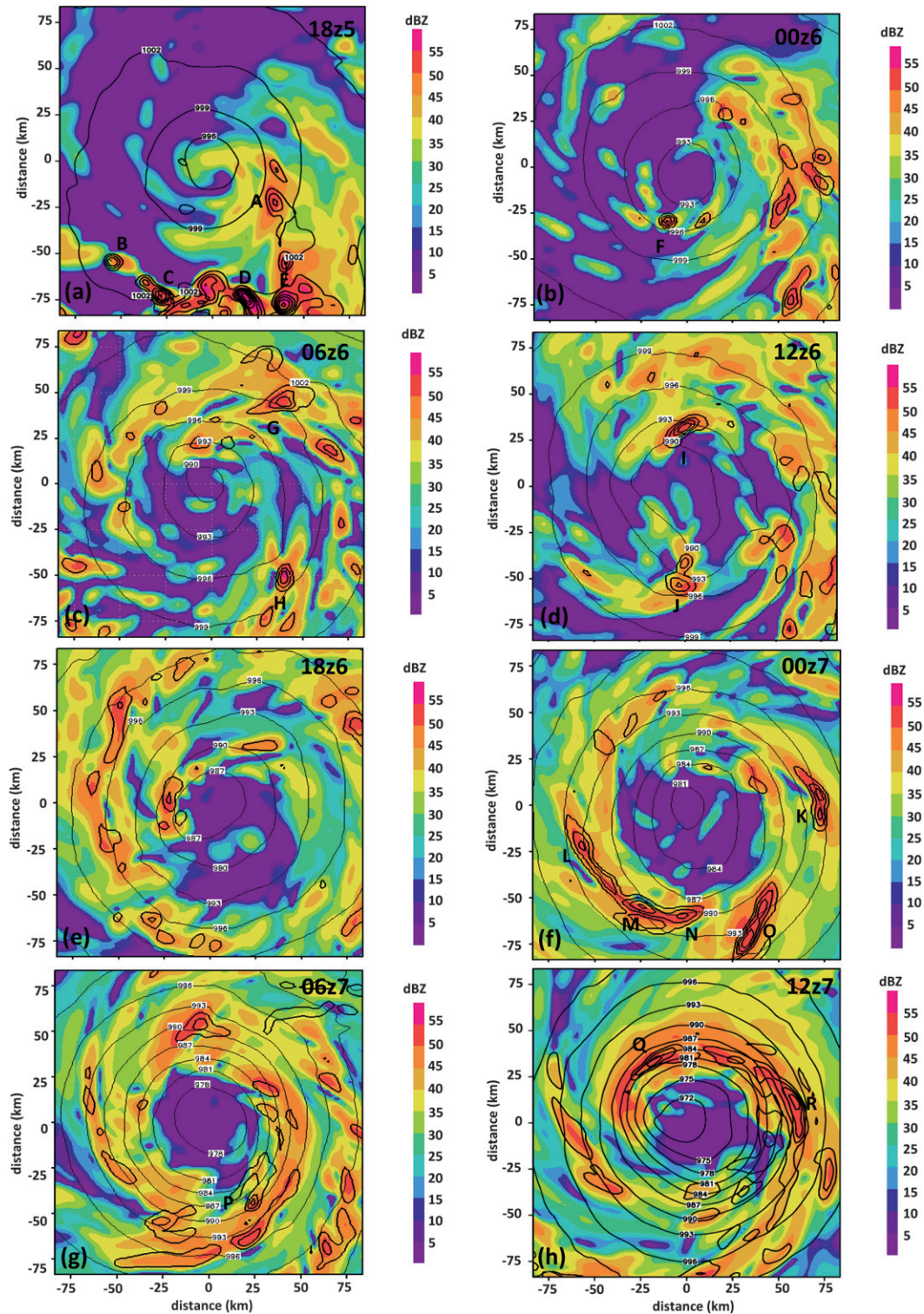
FIG. 5. (a) Model-derived reflectivity (shaded, dB*Z*) at 850 hPa and 700–300-hPa averaged vertical velocity (1, 3, and 5 m s^{-1} contours plotted) at (a) 1800 UTC 5 Jul, (b) 0000 UTC 6 Jul, (c) 0600 UTC 6 Jul, (d) 1200 UTC 6 Jul, (e) 1800 UTC 6 Jul, (f) 0000 UTC 7 Jul, (g) 0600 UTC 7 Jul, and (h) 1200 UTC 7 Jul 205. Letters A–R denote locations of bursts within 75 km of the center identified from the vertical velocity field (discussed later in text).
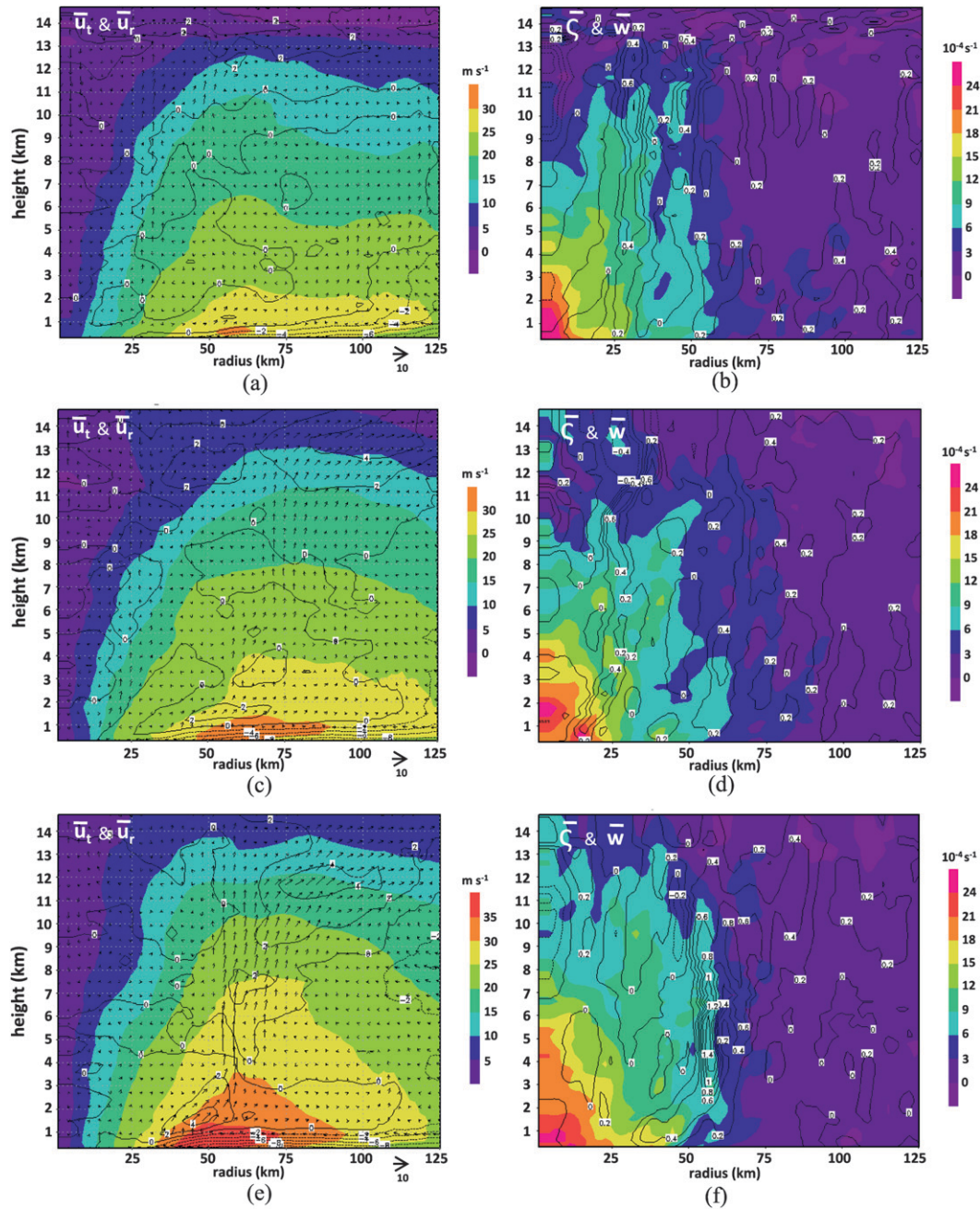
FIG. 6. Radius–height plots of axisymmetric (a) tangential (shaded, m s^{-1}) and radial (contour, m s^{-1}) winds and vectors (m s^{-1}) at 1200 UTC 6 Jul and (b) relative vorticity (shaded, $\times 10^{-4}$ s^{-1}) and vertical velocity (contour, m s^{-1}) at 1200 UTC 6 Jul 2005. (c) As in (a) but at 1800 UTC 6 Jul, (d) as in (b) but at 1800 UTC 6 Jul, (e) as in (a) but at 0000 UTC 7 Jul, and (f) as in (b) but at 0000 UTC 7 Jul.

response to the diabatic heating. These topics are addressed in the following subsections.

a. Convective–stratiform distribution

Figure 8 shows model-derived 850-hPa reflectivity and results from the convective–stratiform partitioning algorithm with 900-hPa vertical motion overlaid. The partitioning does a reasonable job of separating regions into convective and stratiform components based on qualitative comparisons with the reflectivity values. Isolated convective cores are seen at 0600 UTC 6 July, consistent with reflectivity values in excess of ~35 dBZ.
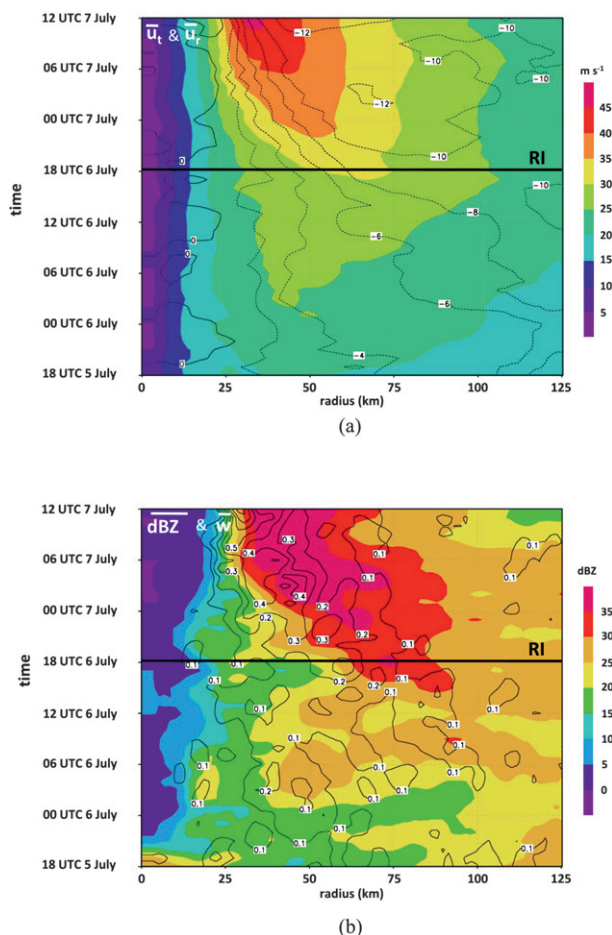
FIG. 7. Time–radius Hovmöller plots of axisymmetric (a) tangential (shaded, m s^{-1}) and radial (contour, m s^{-1}) winds at 0.3-km altitude and (b) reflectivity (shaded, dBZ) at 3-km altitude and vertical velocity (contour, m s^{-1}) averaged in the 0.3–1.5-km layer. Black line denotes the onset of RI.

cipitation prior to RI to a preponderance of convective precipitation after RI has begun.

A vertical cross section through the developing eyewall on the north side of the storm prior to RI (Fig. 9) shows that the areas identified as convective by the partitioning algorithm are dominated by upward motion, high rainwater and graupel mixing ratios, and high reflectivity in the lower troposphere. Peak updrafts of 3 m s^{-1} and reflectivity >45 dBZ are seen along the inner edge of the primary convective region below 600 hPa at 15–30-km distance in Fig. 9a. Weak downdrafts (-0.5 m s^{-1}) are located radially outward from the updraft core within the convective region. Rainwater mixing ratios >1.5 g kg^{-1} and graupel mixing ratios >3 g kg^{-1} are also seen here (Fig. 9b). Outward of this area, stratiform rainfall predominates. Vertical motion is generally weak (<1 m s^{-1}) and the reflectivity low (30–35 dBZ), except for a small area of embedded convective rainfall where the reflectivity exceeds 40 dBZ. Rainwater mixing ratios are about half what they are in the convective region and graupel is limited. Snow is the dominant frozen hydrometeor here, with mixing ratios exceeding 2 g kg^{-1}. This general pattern is consistent with observational studies of rainfall within the inner core of hurricanes (e.g., Marks and Houze 1987; Houze et al. 1992) and previous TC simulations (e.g., Braun 2006; Liu et al. 1997, 1999; Lord et al. 1984).

A time series of the percentage of convective and stratiform grid points within and outside the inner core is shown in Fig. 10. The majority of points are either convective or stratiform, totaling on average between 80% and 90% (the remainder of points are either other or no rain). The percentage of inner-core convective points goes through a distinct evolution: oscillating with a 3–4-h period around 30% from 1800 UTC 5 July to 0900 UTC 6 July, steadily increasing from 0900 to 2100 UTC 6 July, and then oscillating around 50% from 2100 UTC 6 July to 1200 UTC 7 July. While differences in the convective percentages in this study and those of observational studies involving Doppler radar (e.g., Black et al. 1996; Jorgensen et al. 1985) are not surprising because each study uses different vertical velocity and reflectivity thresholds to classify an area as convective, the percentages found here generally fall within the range of Doppler measurements. For example, Black et al. (1996) showed that 14%–40% of the area in the eyewall was convective, while Jorgensen et al. (1985) showed that 37% of the area within a 137-km radius was convective. In contrast to the convective points, the percentage of inner-core points (Fig. 10a) classified as stratiform in the simulation oscillates around 35%–40% for the entire time period. This increase in convective rainfall occurred 3–6 h prior to RI, as shown by the time
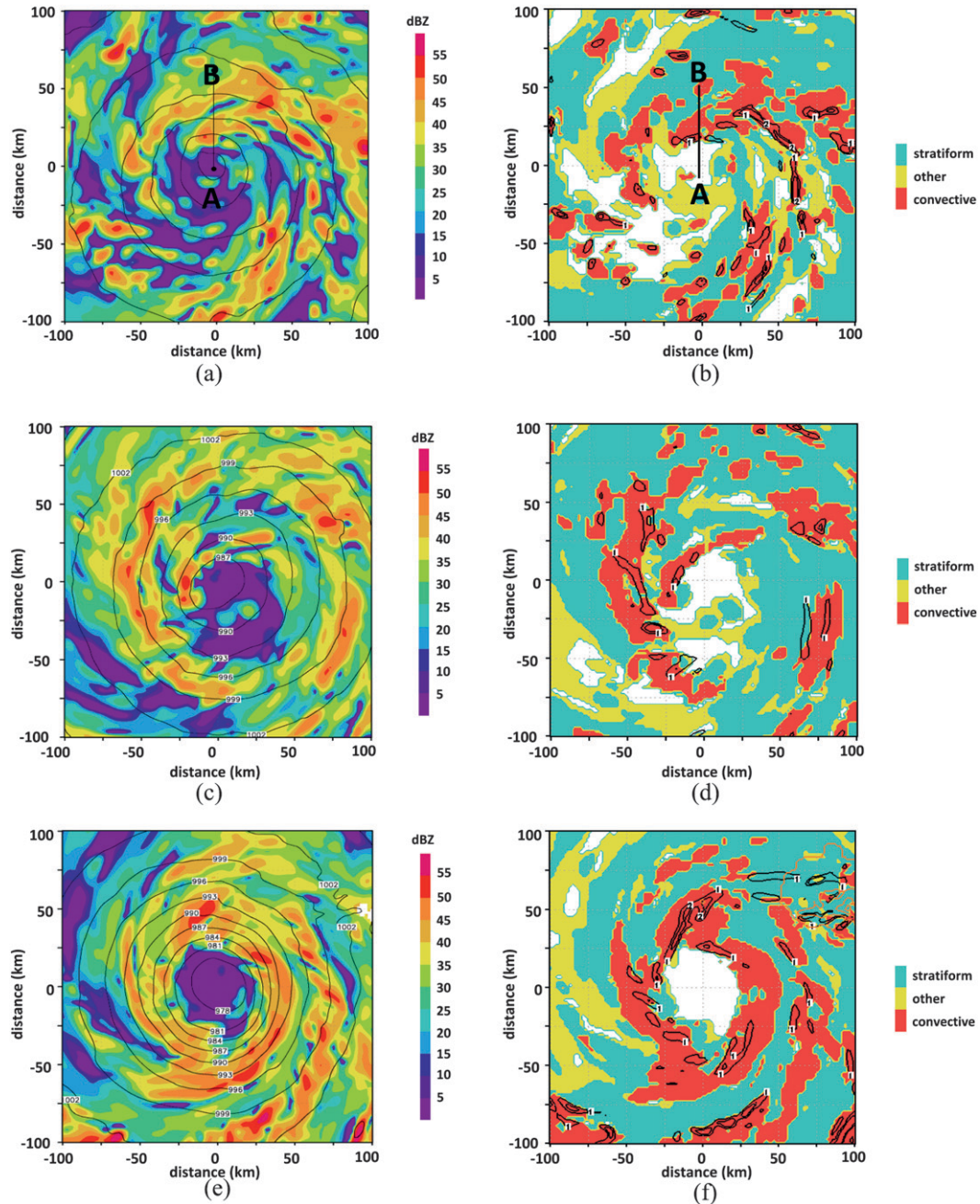
Between those areas lie stratiform precipitation and some regions classified as other. After the storm begins its period of RI, a more coherent ring of convective precipitation is evident on the northwest and west side of the developing eyewall (Figs. 8c and 8d). Stratiform precipitation is dominant on the east side of the circulation at approximately the same radius, but a band of convective precipitation begins on the west side at about 60-km radius and wraps around to the south side. By 0600 UTC 7 July, a well-developed eyewall is evident, composed of a near-solid ring of convective precipitation. A second ring of convective precipitation appears on the east and south side of the center between 60- and 100-km radius. Between these features is stratiform precipitation. Updraft magnitudes of 1–2 m s^{-1} at 900 hPa are primarily located within the convective precipitation at all three times shown. The inner-core precipitation evolves from a mix of convective and stratiform pre-

FIG. 8. (a) Simulated reflectivity (shaded, dBZ) at 850 hPa valid 0600 UTC 6 Jul 2005. (b) Results of the convective–stratiform partitioning algorithm (shading) and 900-hPa vertical velocity (contour, 1 and 2 m s^{-1} values contoured). (c) As in (a) but at 1800 UTC 6 Jul, (d) as in (b) but at 1800 UTC 6 Jul, (e) as in (a) but at 0600 UTC 7 Jul, and (f) as in (b) but at 0600 UTC 7 Jul. Lines A–B in (a) and (b) denote locations of cross section shown in Fig. 9.

series of smoothed peak surface winds taken from Fig. 1b. Outside of the inner core (Fig. 10b), stratiform rain is much more prevalent, with percentages between 50% and 60% for much of the time, compared with about 20% for the convective precipitation. Reductions in the percentages of the convective area in the outer regions

are seen in the observational studies of Black et al. (1996) and Jorgensen et al. (1985). Both convective and stratiform rain outside the inner core show little change in their percentages over time. It thus appears that the onset of RI in this simulation is most closely tied to an increase in the percentage of convective rainfall within
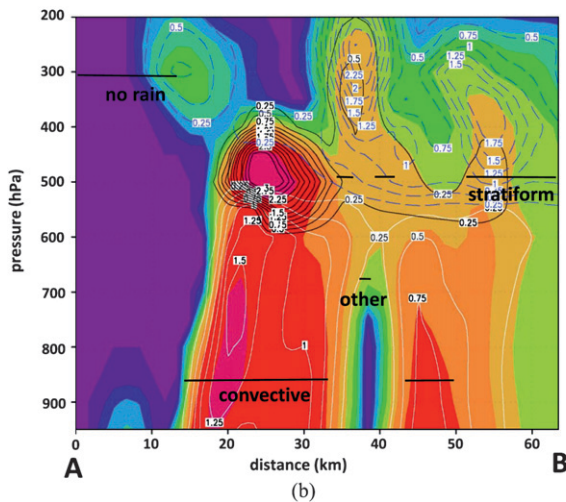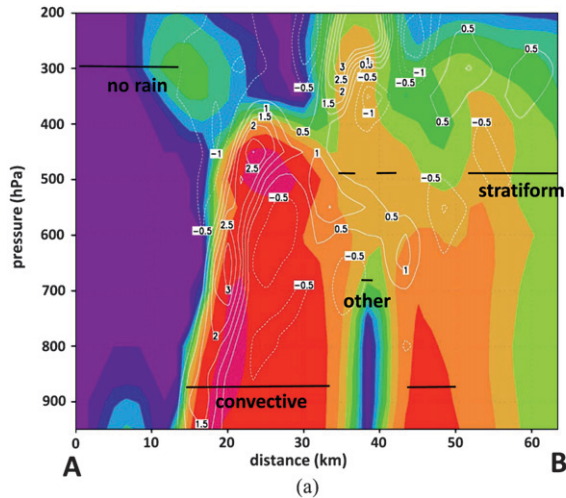
FIG. 9. (a) Vertical cross section of reflectivity (shaded, dBZ) and vertical velocity (contour, m s^{-1}) along line A–B in Fig. 8. (b) Vertical cross section of reflectivity (shaded), rainwater mixing ratio (white contour, g kg^{-1}), graupel mixing ratio (black contour, g kg^{-1}), and snow mixing ratio (blue dashed contour, g kg^{-1}). Areas classified as convective, stratiform, other, and no rain are indicated.
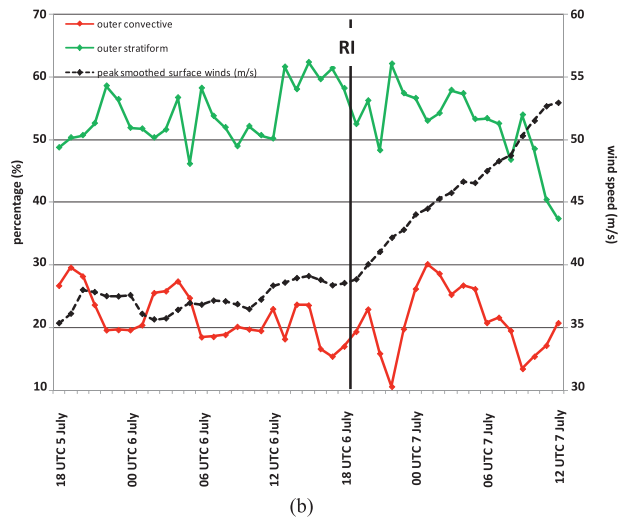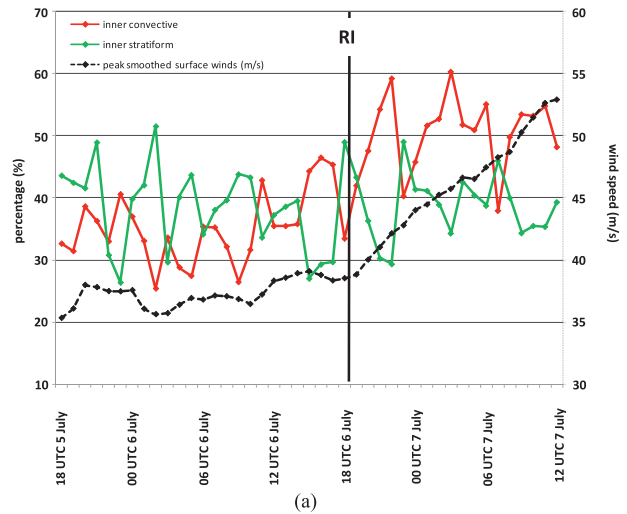

FIG. 10. (a) Time series of the percentage of points within the inner 75 km classified as convective (red) and stratiform (green). Black dashed line shows the simulated peak surface winds smoothed over a 5-h period as in Fig. 1. (b) As in (a) but for points outside of 75 km. Black line denotes the onset of RI.

the inner core. For this reason the rest of the discussion will focus on the inner core.

Time–height series of areally averaged vertical motion, horizontal divergence, and potential vorticity for the inner-core convective and stratiform regions are shown in Fig. 11. The general shape of the mean vertical motion profile—a single updraft peak at ~4 km altitude for the convective region and an 10–12-km updraft peak and 4-km downdraft peak for the stratiform region—is consistent with past studies of convective–stratiform structures in tropical and midlatitude mesoscale convective systems (e.g., Houze 1977; Zipser 1977; Gamache and Houze 1982; Johnson 1984; Mapes and Houze 1995)

and tropical cyclones (Marks and Houze 1987; Black et al. 1996). The mean convective vertical velocity profile evolves from a layer of updrafts >0.5 m s^{-1} between 2- and 4-km altitude prior to the onset of RI to an updraft layer extending from 2- to 10-km altitude after RI has begun. These deeper updrafts are likely tied to the establishment of a well-defined secondary circulation (cf. Fig. 6). Periods of strong convective updrafts occur both before and during RI. The mean stratiform vertical velocity profile also shows intermittent maxima in the 10–12-km layer that steadily increase after RI has begun. Stratiform downdrafts, maximized at around 3–4-km altitude, vary between −0.1 and −0.2 m s^{-1} during the time period and show no discernible trend in magnitude
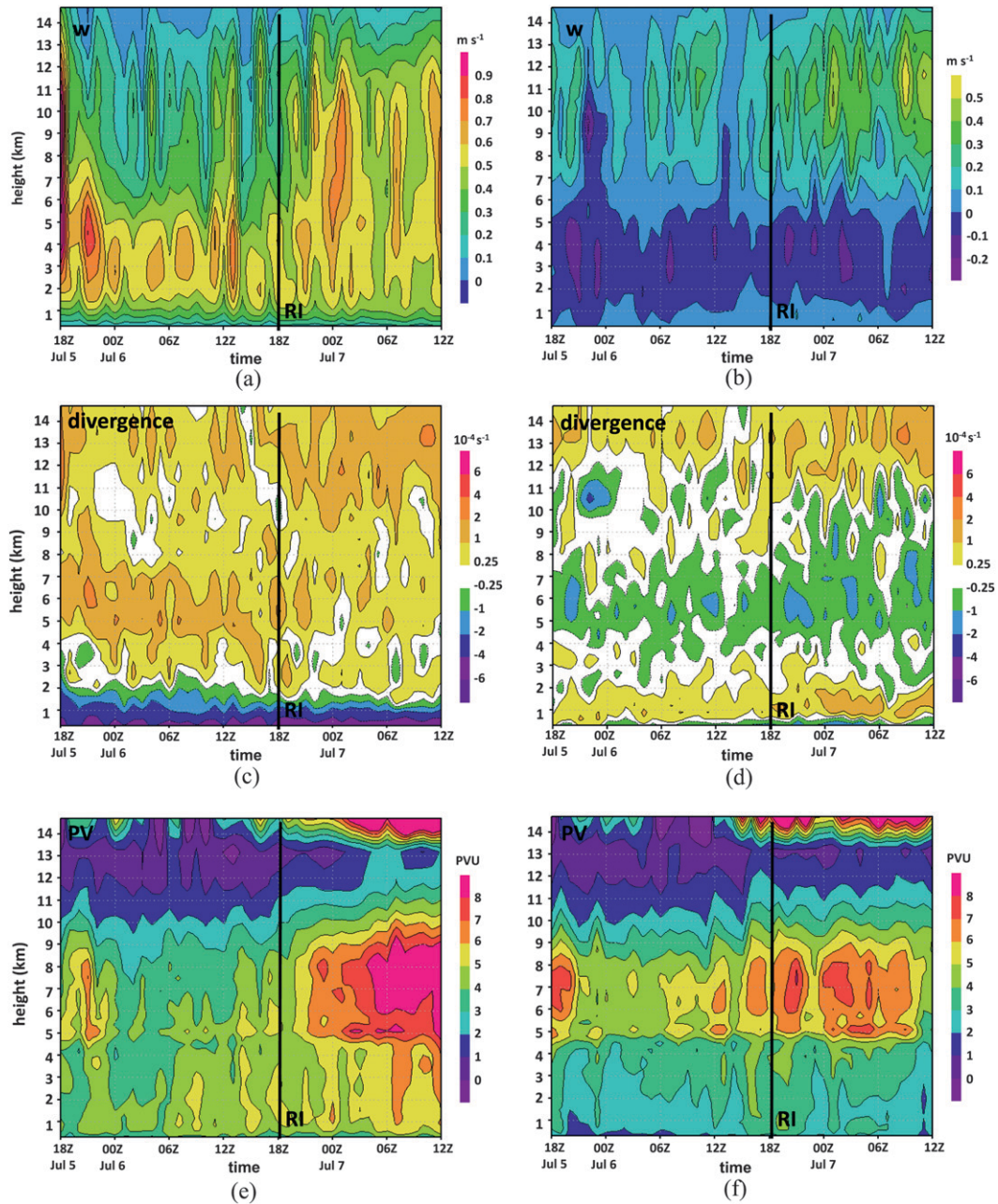
FIG. 11. (a) Time–height series from 1800 UTC 5 Jul to 1200 UTC 7 Jul 2005 of the mean vertical velocity (shaded, m s^{-1}) in convective regions within the inner 75 km. (b) As in (b) but for stratiform regions, (c) as in (a) but for horizontal divergence (shaded, 10^{-4} s^{-1}), (d) as in (c) but for stratiform regions, (e) as in (a) but for potential vorticity (shaded, PVU), and (f) as in (e) but for stratiform regions. Black line denotes the onset of RI.

or shape. This lack of temporal variability in downdraft magnitude and shape has been shown in other studies [e.g., in idealized tropical cyclogenesis simulations (Nolan 2007)].

Similar to the vertical velocity profiles, the divergence evolution (Figs. 11c and 11d) shows significant differences between the convective and stratiform regions.

For the convective regions there is strong convergence in the lowest 2 km. Prior to the onset of RI, divergence in the convective regions is maximized between 5 and 7 km, at the top of the vertical motion peak in Fig. 11a. After RI, the divergence in the convective regions is peaked at 12–14-km altitude. The stratiform regions show the typical divergence profile seen in tropical and

midlatitude MCSs (see same references as above): low-level divergence between 0.5- and 3-km altitude, mid-level convergence between 4- and 7-km altitude, and upper-level divergence above 10–11 km. There is no discernible trend in the stratiform divergence profiles prior to and during the onset of RI; after RI begins, the divergence in the stratiform region at 1–2-km altitude amplifies. The convective and stratiform mean divergence profiles shown in Figs. 11c and 11d result in the evolution of the potential vorticity (PV) shown in Figs. 11e and 11f. In the convective region, the PV is maximized in the 1–3-km layer 12–18 h prior to the onset of RI. Intermittent periods of increased low-level PV occur around 0900 and 1500 UTC 6 July. This pattern continues until the onset of RI, when the PV becomes maximized between 5- and 10-km altitude. The midlevel PV maximum in the convective regions after RI onset likely reflects the amplification of the vortex as a whole, similar to the vertical velocity evolution described above (cf. Fig. 11a). In the stratiform region, the PV remains maximized in the 5–10-km layer during the entire time shown here. The PV in the stratiform region increases in the lower troposphere (between 1- and 4-km altitude) in the 6–12-h time period prior to RI onset. The relationship between vertical velocity, divergence, and PV evolution prior to RI supports the work of Hertenstein and Schubert (1991) and Tory et al. (2006), who found that the stratiform region primarily enhances PV in the middle levels, while the convective region enhances PV in the lower troposphere.

b. Convective bursts

The time–height series in Fig. 11 show intermittent periods of strong mean 2–10-km inner-core upward motion. These time periods correspond to the occurrence of vigorous convection, defined as where the layer-averaged vertical velocity within the middle troposphere (700–300 hPa) exceeds 5 m s^{-1}. Typically representing the top 1%–2% of the updraft distributions in this layer (e.g., Black et al. 1996), this is the threshold for identifying the presence of a convective burst in the simulation. This is broadly consistent with past observational studies [e.g., Reasor et al. (2009), who defined a burst as when the 2–6-km layer-average updraft was >5 m s^{-1} and the 2-km reflectivity was >30 dBZ] and modeling studies [e.g., Montgomery et al. (2006), who defined a model hot tower as being where updrafts were >1 m s^{-1} from 1- to 15-km altitude]. An hourly time series of the number of bursts within the inner core between 1800 UTC 5 July and 1200 UTC 7 July (Fig. 12a) shows that the number of bursts varies between zero and five at
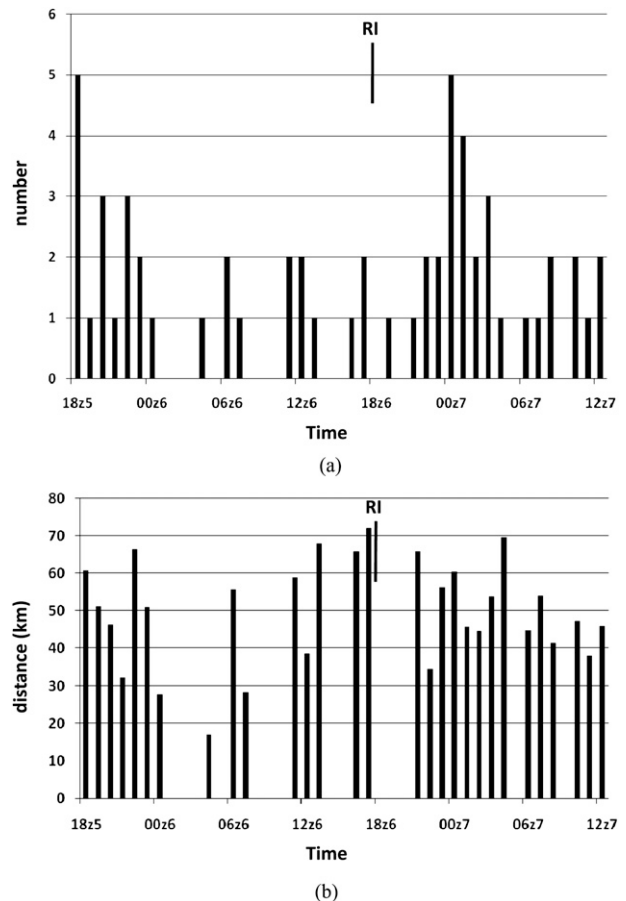

FIG. 12. (a) Time series from 1800 UTC 5 Jul to 1200 UTC 7 Jul 2005 of the number of bursts within inner 75 km of the storm center. (b) Time series of the average distance (km) from the storm center of bursts. Black line denotes the onset of RI.

any given output time[2], with two predominant peaks evident between 1800 and 2200 UTC 5 July and 0000 and 0300 UTC 7 July. Outside of these times, the distribution of bursts is fairly even: some times have no bursts, while others have one or two bursts. There is no obvious indication of a dramatic increase in burst numbers within the 18 h prior to the onset of RI. The average distance of the bursts from the storm center (Fig. 12b) shows significant variability, ranging between 40 and 70 km from hour to hour (e.g., at 1200–1300 UTC 6 July).

---

[2] Past modeling studies involving convective bursts at comparable resolution (e.g., Montgomery et al. 2006) found that the average life spans of these bursts are on the order of 1 h, though on occasion some did persist for up to 3 h. So it is possible that some of the bursts counted in Fig. 12 are not distinct and new events and thus may be double-counted. However, it is not felt that this is a significant fraction of the bursts, and the cases where bursts did persist for >1 h do not invalidate the analyses to follow.

Examples of these bursts and the vortex structure prior to and during RI are seen in Figs. 5 and 13, which show the reflectivity and PV, respectively, at the 850-hPa and midlevel (700–300 hPa averaged) vertical motions from 0000 UTC 6 July to 0600 UTC 7 July. Prior to 0000 UTC 6 July (Fig. 5a), precipitation is concentrated on the east side in the inner core. Bursts continue to develop within the bands of precipitation that wrap around the center and form the eyewall by 0000 UTC 7 July, though the bursts occupy a small percentage of the precipitating area. The PV at 0000 UTC 6 July (Fig. 13) is concentrated in the inner 25 km of what will become the eye. Scattered areas of high PV are also found in the precipitation on the east side of the storm, as well as a core of high-PV air collocated with burst A. The magnitude of the PV in the incipient eye remains ~20 PV units (PVU, where 1 PVU = 1.0×10^{-6} m^2 s^{-1} K kg^{-1}) and the areal extent of the high-PV air remains approximately constant during the 18 h prior to RI onset. Once RI has begun, the areal extent of high-PV air in the eye increases (e.g., at 0600 UTC 7 July; see Fig. 13g). Outside of the inner PV maximum associated with the eye, PV in the precipitating regions increases in coverage during the 30 h shown here, including the 18 h prior to RI. The increasing 850-hPa PV in the precipitating areas is consistent with the increase in lower-tropospheric PV seen in both the convective and stratiform areas prior to RI shown in Fig. 11. The bursts shown in Fig. 13 are generally located near regions of enhanced positive and negative PV, suggesting that these features are generating PV anomalies and are related to vortical hot towers (VHTs; Hendricks et al. 2004; Montgomery et al. 2006).

Figure 14 provides a more detailed look at the statistical properties of the bursts by showing contoured frequency by altitude diagrams (CFADs; Yuter and Houze 1995) of the vertical motion and reflectivity in the inner-core convective regions. Three separate composites are created for the comparisons: one consisting of three times prior to the onset of RI where there were no bursts, one with times prior to RI where there were at least three bursts identified, and a third with times after the onset of RI where at least three bursts were identified. These comparisons will show if there are any differences in the microphysical variables at burst versus no-burst times and if there are differences between burst times prior to RI and burst times during RI. A comparison of the vertical velocity CFADs (Figs. 14a, 14c, and 14e) shows several differences between the burst times (both pre-RI and RI) and the nonburst times. The distributions are broader for the burst times, with peak updrafts of 15–18 m s^{-1} and downdrafts of 6–7 m s^{-1} compared with updraft peaks of 10–12 m s^{-1} and downdraft peaks

of −4 m s^{-1} for the nonburst times. Additionally, the burst times show updraft maxima at 5- and 9-km altitude for the 2%–5% contour level, corresponding to 3 m s^{-1} for these distributions. These bimodal updraft profiles have been seen in the observations and simulations of tropical convection and TCs (e.g., Black et al. 1996; May and Rajopadhyaya 1996; Zipser 2003; Fierro et al. 2008, 2009, hereafter AOF) and have been attributed to frictional convergence (for the lower peak) and water unloading and buoyancy (for the upper peak). While notable differences exist in the vertical velocity CFADs between burst and nonburst times, the differences between the pre-RI and RI burst times are much smaller. Peak updrafts (top 0.1%) in the 1–4-km layer are stronger during the pre-RI times, while peak up- and downdrafts (top and bottom 0.01%) are stronger in the 10–14-km layer during the RI times. In general, though, the vertical velocity statistics are very similar for convective bursts prior to and during RI.

For the reflectivity CFADs (Figs. 14b, 14d, and 14f), three primary differences exist between the burst and nonburst times. First, modal values are about 5 dBZ lower for the nonburst times compared to the burst times, particularly in the lower troposphere. Second, a region of enhanced reflectivity above the melting layer (around 6-km altitude) is more pronounced for the burst times compared to the nonburst times. This region, clearly seen in the 2%–5% contour, is likely due to enhanced graupel concentrations (not shown) supported by the stronger low-level updrafts during the burst times. Finally, in the 10–14-km layer there is a higher percentage of points with high reflectivity for the burst times compared with the nonburst times. For example, at 12-km altitude there are no points during the nonburst times experiencing reflectivity as high as 35 dBZ. By contrast, for the burst times 1%–2% of the points are experiencing reflectivity of this magnitude. Similar to the vertical velocity CFADs, there is very little difference in the pre-RI and RI reflectivities, except for higher peak (top 1%) reflectivity in the 1–4-km layer for the pre-RI bursts.

While little difference is seen in the convective statistics for pre-RI and RI bursts, some differences are seen in the potential vorticity structures for the two time composites shown in Figs. 14c–e. Figure 15 shows the PV for the inner-core convective regions averaged within vertical velocity bins for the pre-RI and RI composite times shown in Fig. 14. For both the pre-RI and RI times, peak PV is associated with the strongest vertical velocities, providing further evidence that the strongest updrafts are VHTs. However, the magnitude of the peak PV for the RI times is higher than the pre-RI times by a factor of 3–4, and the 10-PVU contour extends up to 12 km for the RI times compared to 8 km for the pre-RI
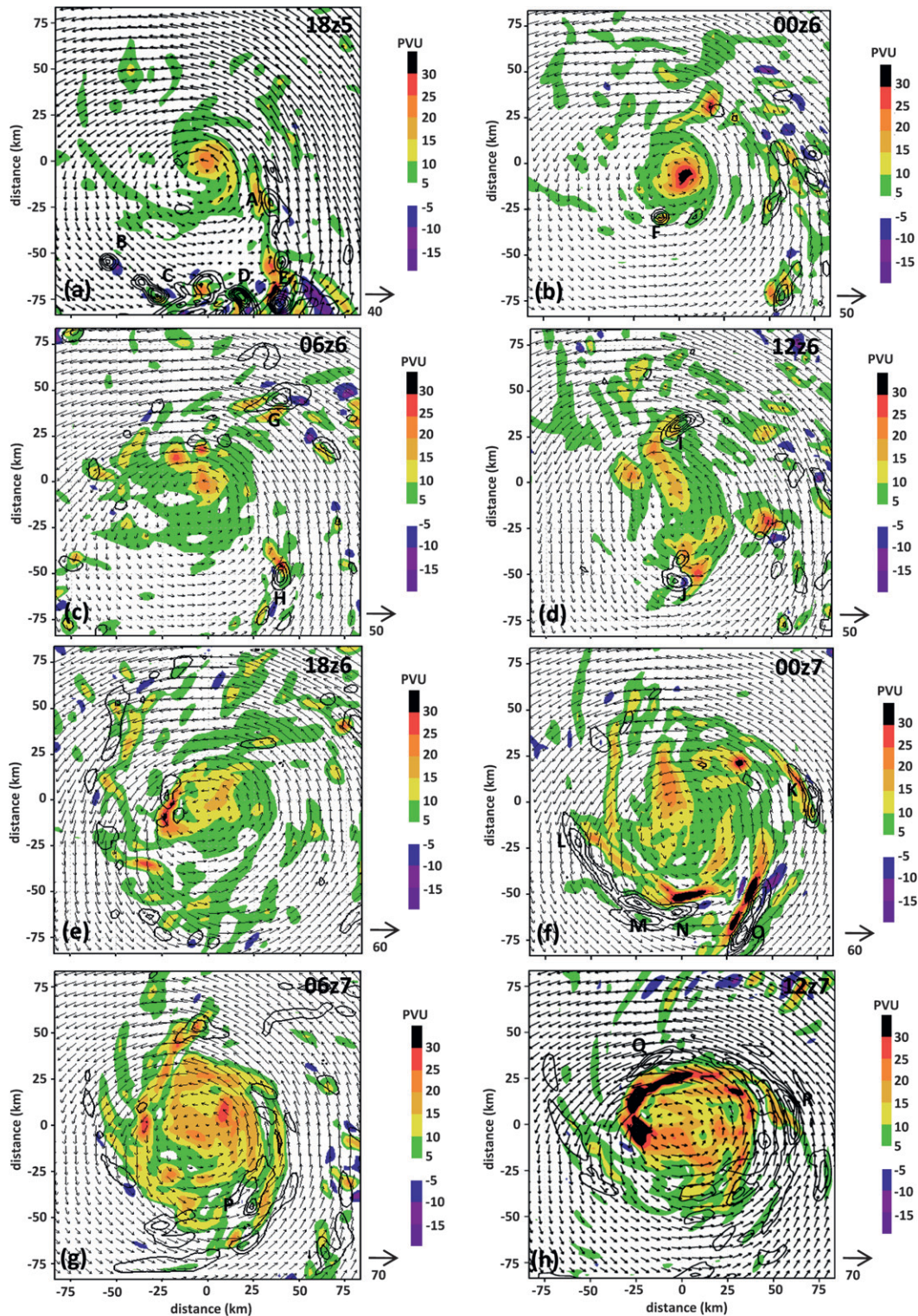
FIG. 13. (a) Model-derived potential vorticity (shaded, PVU) at 850 hPa, vertical velocity averaged in the 700–300-hPa layer (contour, 1, 3, and 5 m s^{-1} contours plotted), and 850-hPa winds (vectors, m s^{-1}) at (a) 1800 UTC 5 Jul, (b) 0000 UTC 6 Jul, (c) 0600 UTC 6 Jul, (d) 1200 UTC 6 Jul, (e) 1800 UTC 6 Jul, (f) 0000 UTC 7 Jul, (g) 0600 UTC 7 Jul, and (h) 1200 UTC 7 Jul 2005. Letters A–R denote locations of bursts within 75 km of the center identified from the vertical velocity field.
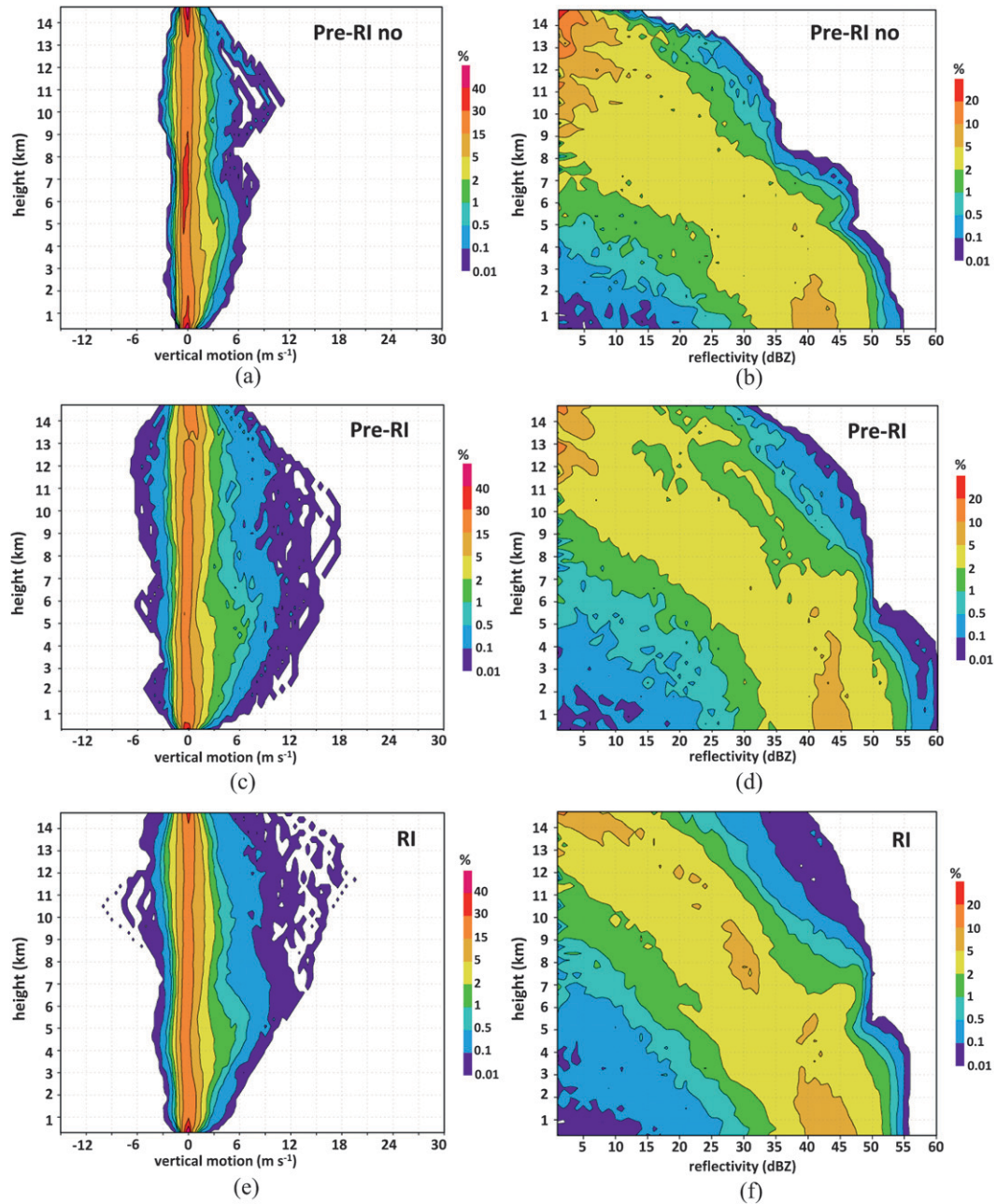
Fig. 14. (a) Composite CFAD (shading, %) of the vertical velocity for times prior to RI during which no bursts occurred (0100, 0200, and 0300 UTC 6 Jul 2005). (b) As in (a) but for model-derived reflectivity, (c) as in (a) but for times when bursts occurred prior to RI (1800, 2000, and 2200 UTC 5 Jul), (d) as in (c) but for reflectivity, (e) as in (a) but for times when bursts occurred during RI (0000, 0100, and 0300 UTC 7 Jul), and (f) as in (e) but for reflectivity.

times. Since the vertical velocity and reflectivity statistics during the pre-RI and RI times are essentially unchanged (cf. Fig. 14), the differences seen in Fig. 15 do not reflect fundamental differences in the convective-scale structures of the bursts prior to and during RI. Rather, they are likely due to the fact that the inner-core vorticity is amplifying and expanding over time (cf. Figs. 6

and 13) and there is a stronger phasing between updrafts and positive vorticity (and PV).

c. Vortex-scale response

As highlighted by Ooyama (1982), vortex intensification is ultimately tied to increasing net mass flux within the inner core driven by an amplifying secondary circulation,
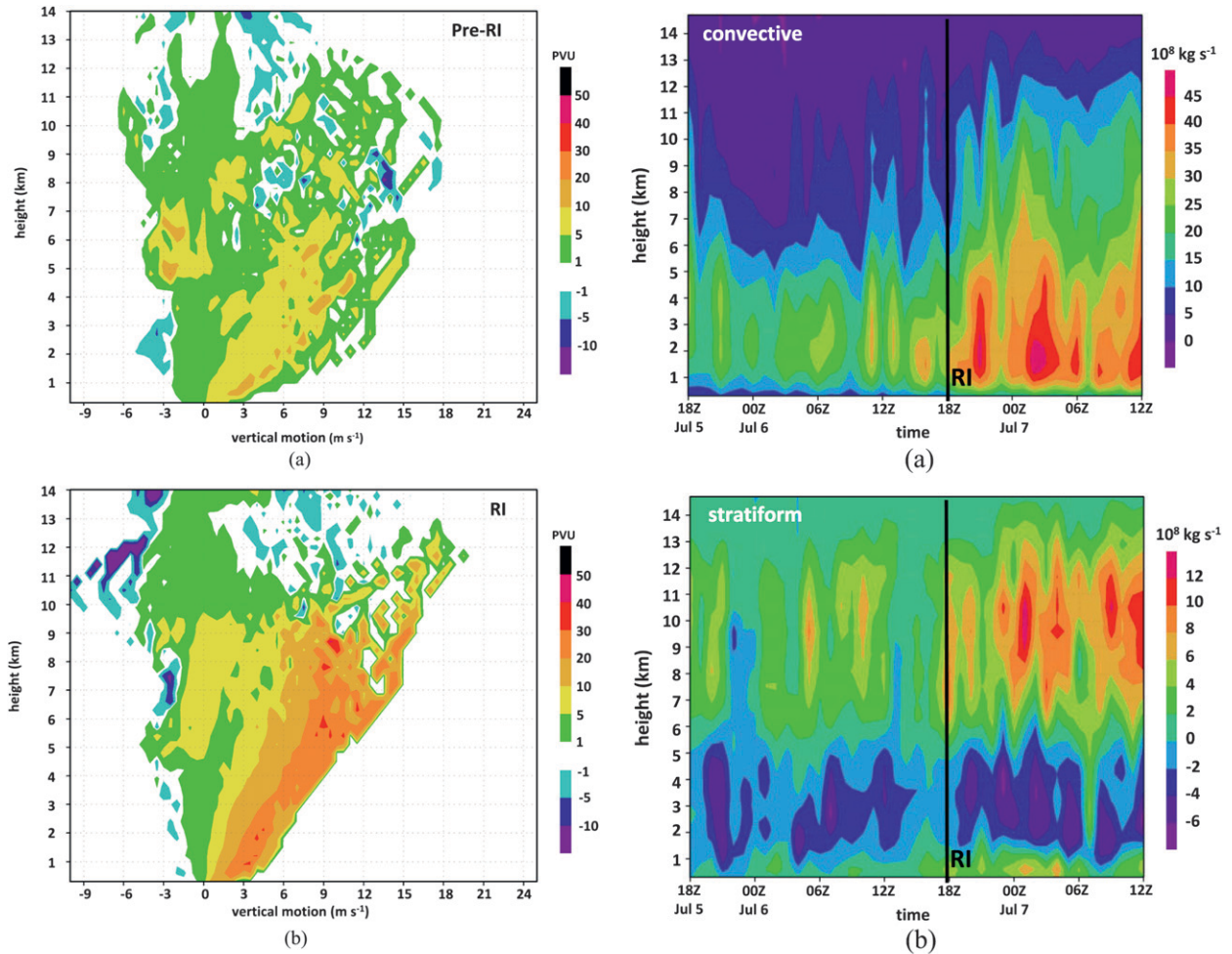
FIG. 15. (a) Composite vertical velocity-binned mean potential vorticity (shaded, PVU) for times when bursts occurred prior to RI (1800, 2000, and 2200 UTC 5 Jul 2005). (b) As in (a) but for times when bursts occurred during RI (0000, 0100, and 0300 UTC 7 Jul).

composed of a deep-layer radial inflow and upward motion in the ascending branch of the circulation. Figure 16 shows a time–height series of the convective, stratiform, and total (convective, stratiform, other, and no rain) inner-core net vertical mass flux. Upward net mass flux in the convective regions is maximized in the lowest 4 km for the time prior to RI, beginning its increase prior to RI at 1200 UTC 6 July. After RI has begun, both the magnitude and the depth of the peak convective net mass flux increase. For the stratiform regions, the upward motion peak at 10–12 km results in a much smaller contribution to the net mass flux. Weak downward mass flux is also seen in the 1–4-km layer in the stratiform regions associated with mesoscale subsidence. This negative stratiform net mass flux is easily compensated for by the positive convective net mass flux, however. The total net mass flux (Fig. 16c) is very similar to the
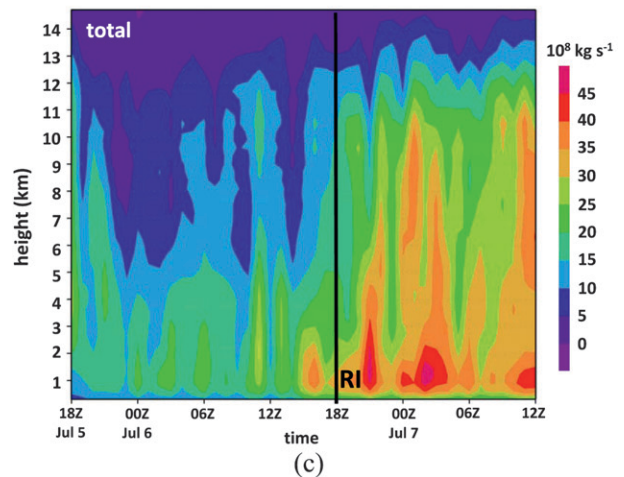

FIG. 16. (a) Time–height series from 1800 UTC 5 Jul to 1200 UTC 7 Jul 2005 of mass flux (shaded, 10^8 kg s^{-1}) in convective regions within the inner 75 km. (b) As in (a) but for stratiform regions within the inner 75 km. (c) As in (a) but for all regions within the inner 75 km. Note differences in scale. Black line denotes the onset of RI.

convective mass flux, even though nearly equal numbers of points are stratiform as convective in the inner core (cf. Fig. 10). Peak values of total net mass flux prior to RI are 35×10^8 kg s^{-1}, which is comparable in magnitude to that obtained by AOF for a 60-km radius area at 1.1-km altitude around the center of a Hurricane Rita (2005) simulation. The peak values shown here are about an order of magnitude smaller than those in Black et al. (1996), though, as pointed out by AOF, this difference may be because Black et al. scaled their calculation by 2π. A significant (50%–75%) increase in total mass flux in the 1–2-km-altitude layer occurs from 1400 to 1600 UTC 6 July, 4 h prior to RI. Note that this time does not correspond to a significant increase in the number of convective bursts (cf. Fig. 12).

While the onset of RI is most closely linked to the rapid increase in total vertical mass flux in the lowest 1–2 km, what is not known is which part of the updraft spectrum is primarily responsible for this increase. In other words, is this mass flux increase related to increases in weak drafts covering a large area or strong drafts covering a small area? Answering this question can provide insight into the role of convective bursts in causing RI. Figure 17 shows a time–height series of the areal coverage of inner-core updrafts falling within three thresholds: weak/moderate (1–2 m s^{-1}, representing ~15%–30% of the total vertical velocity distribution), moderate/strong (5–6 m s^{-1}, ~1%–2% of the distribution), and strong/extreme (10–11 m s^{-1}, ~0.01–0.1% of the distribution). There are two periods where a significant portion of the 8–14-km layer is covered by weak/moderate drafts (Fig. 17a): between 1800 UTC 5 July and 0000 UTC 6 July and after 1800 UTC 6 July. For the lowest 2-km altitude, the areal coverage of these drafts remains around 4%–6% until 1500 UTC 6 July, 3 h prior to the onset of RI. At that time the coverage nearly doubles to >8%. For the moderate/strong drafts, corresponding to the lower 5 m s^{-1} threshold for convective bursts (Fig. 17b), there are times of increased areal coverage in the 4–6-km altitude range that are coincident with the times when most convective bursts occurred (e.g., 1800 UTC 5 July–0000 UTC 6 July, ~1200 UTC 6 July, after 1800 UTC 6 July; cf. Figs. 5, 12, and 13). A marked and persistent increase to >1% coverage occurs in the midlevels for the moderate/strong drafts after RI has begun. For the strong/extreme drafts (Fig. 17c), there is no clear relationship in the timing of the drafts and the timing of RI. From these comparisons it appears that the temporal evolution of the areal coverage of weak/moderate drafts, in particular in the lower troposphere, is most closely tied to the onset of RI.

The contributions of different vertical velocities to the total inner-core vertical mass flux at 1.5-, 5.1-, and 9.9-km
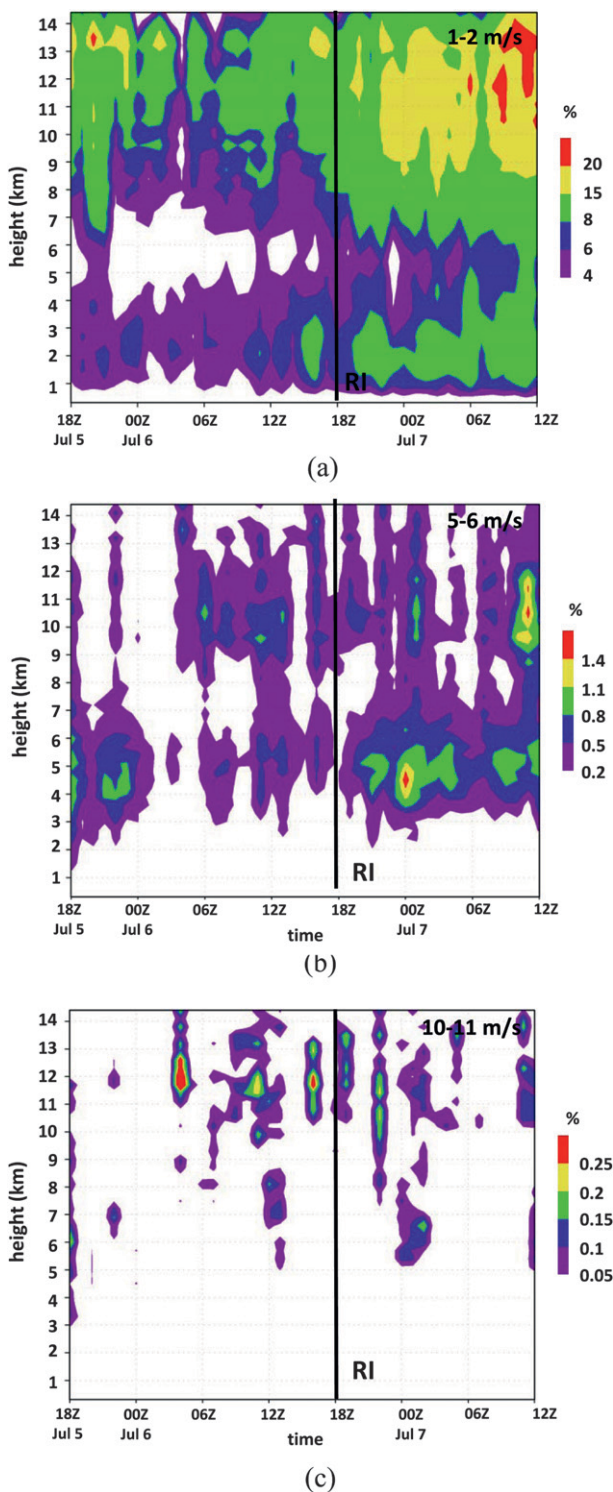

FIG. 17. Time–height series from 1800 UTC 5 Jul to 1200 UTC 7 Jul 2005 of percentage of total area (shaded, %) within the inner 75 km with vertical velocities in various ranges. (a) Values of w between 1 and 2, (b) 5 and 6, and (c) 10 and 11 m s^{-1}. Black line denotes the onset of RI.
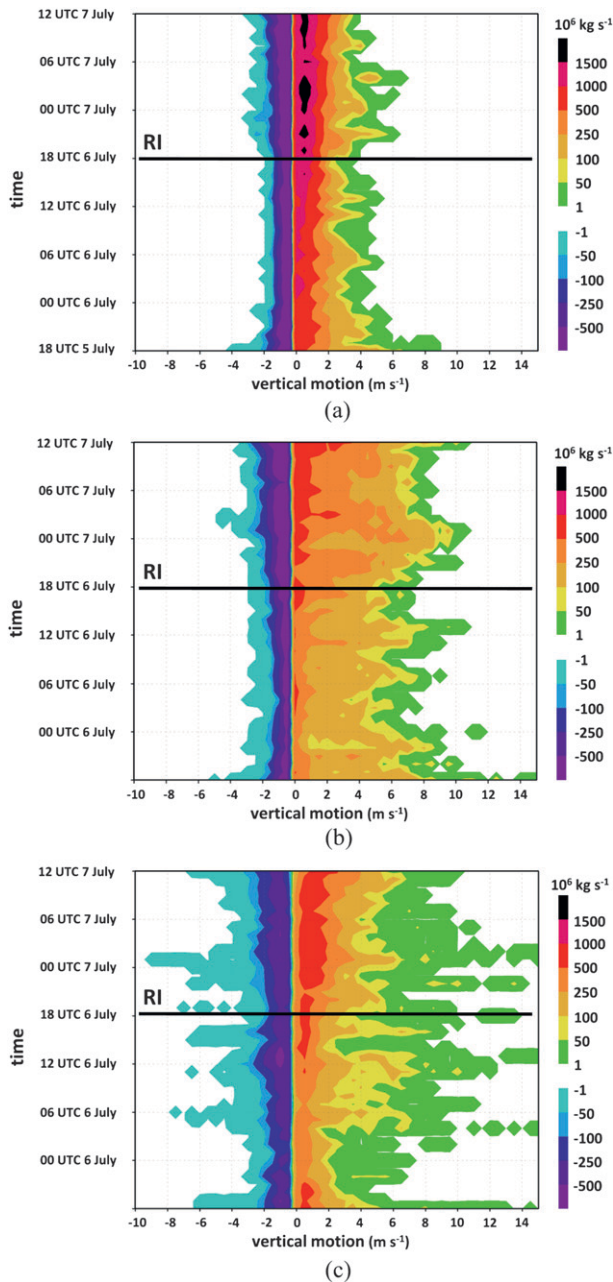
FIG. 18. Time series of vertical velocity-binned aggregate mass flux (shaded, 10^6 kg s^{-1}) at (a) 1.5-, (b) 5.1-, and (c) 9.9-km altitudes. Black line denotes the onset of RI.

FIG. 19. (a) Time series of total inner-core updraft mass flux (10^6 kg s^{-1}). (b) Time series of proportion (%) of updraft mass flux contributed by drafts $\geq$5 m s^{-1}. Black line denotes the onset of RI.

altitudes and how they vary over time are shown in Fig. 18. At all three levels, the bulk of the mass flux (both upward and downward) is concentrated in the weak/moderate draft range. This is consistent with the radar studies of Florida cumulonimbus by Yuter and Houze (1995), who found that the more numerous weak and moderate-strength drafts accomplished most of the vertical mass transport. In addition, it is this range of updraft
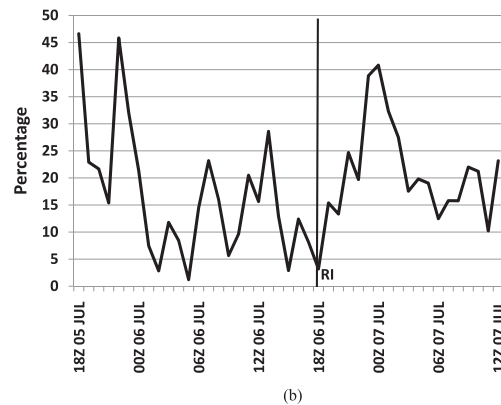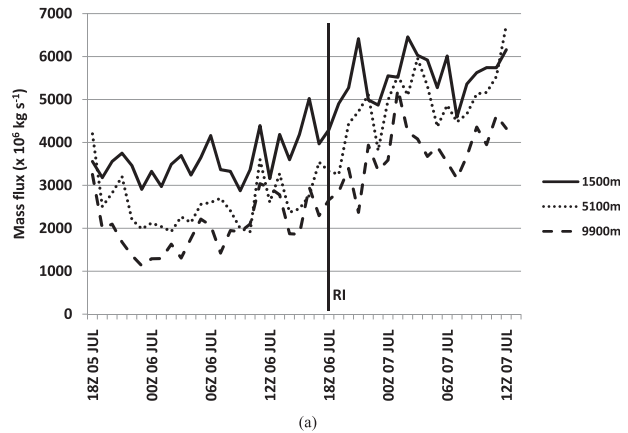
magnitudes whose temporal evolutions most closely follow the intensification of the TC. At 1.5 km, updraft mass flux for the 1 m s^{-1} bin increases from 500 to 1000 $\times$ 10^6 kg s^{-1} between 1200 and 1800 UTC 6 July. Conversely, the stronger updrafts (3 m s^{-1} at this altitude) contribute only ~100 $\times$ 10^6 kg s^{-1} to the vertical mass flux, and there is no clear trend in the amount contributed by this updraft range prior to 1800 UTC 6 July. No trend is evident in the contribution from low- to midlevel downdrafts. At 5.1 km (Fig. 18b), a trend toward higher contributions from updrafts in the 2–5 m s^{-1} range is evident, but this increase does not occur until after RI at 1800 UTC 6 July. Similar to the 1.5-km level, the majority of the upward mass flux and mass flux increase is accomplished by the weak/moderate drafts. At 9.9 km, the downdraft mass flux shows a significant (and transient) increase in the mass flux produced by the 1–2 m s^{-1} downdrafts at around 1200 UTC 6 July.

The relative role of strong versus weak updrafts in determining the evolution of the total updraft mass flux is shown in Fig. 19, which shows time series of the total updraft mass flux and the proportion of updraft mass

flux accomplished by drafts ≥ 5 m s^{-1} at 5.1-km altitude. Consistent with Fig. 16, the updraft mass flux is highest at 1.5-km altitude. The magnitude at 1.5 km remains $\sim 3500 \times 10^6$ kg s^{-1} until 1200 UTC 6 July, at which point a steady increase to $\sim 5000 \times 10^6$ kg s^{-1} occurs by 2100 UTC. At 5.1-km altitude, there is an enhancement in the mass flux around 1200 UTC 6 July, but then it decreases again until a more steady increase occurs as RI begins. These increases at the higher altitudes as RI begins are delayed 3–6 h compared to the increase at 1.5 km. The proportion of updraft mass flux contributed by drafts ≥ 5 m s^{-1} at 5.1 km (Fig. 19b) shows the contribution of the convective bursts to the total upward flux. The contribution varies between 0% and 45%, with an average of 20% during the time period. The timing of the peaks corresponds with the timing of the bursts (cf. Fig. 12a). These values, consistent with the modeling studies of Braun (2002, 2006) and AOF, indicate that updraft cores that occupy 1%–4% of the inner core typically accomplish 20% of the total updraft mass flux, with some isolated times of up to 40%–45% possible. From Fig. 19, it appears that the period of enhanced updraft mass flux at 5.1 km between 0600 and 1200 UTC 6 July is related to the onset of RI, but not directly. Rather, low-level (1.5 km) updraft mass flux begins its increase at 1200 UTC, near the end of the period of enhanced midlevel contribution seen in Fig. 19b. Furthermore, the bulk of this increase in the low-level upward flux is accomplished by the weak/moderate drafts, not the strongest drafts (cf. Fig. 18a). The convective bursts between 0600 and 1200 UTC 6 July lead to a response from the vortex manifested as a steady increase in the low-level updraft mass flux from the weak/moderate drafts (i.e., the drafts ≤ 1–2 m s^{-1}). Once the low-level updraft mass flux increases, RI begins.

An examination of the evolution of downdraft mass flux is also important to gain a more complete picture of the convective- and vortex-scale processes that are important for RI. The transient increase in downdraft mass flux at 9.9 km at 1200 UTC 6 July produces enhanced subsidence warming, and, when produced by inner-core convection, these downdraft mass flux increases can cause a hydrostatic pressure decrease and vortex amplification (Shapiro and Willoughby 1982). Heymsfield et al. (2001) presented evidence that convective bursts can generate locally strong downdrafts and a net adiabatic warming within the eye. Figure 20a shows a time series of the downdraft mass flux for the no-rain areas, which provides a good approximation for the eye, at 1.5-, 5.1-, and 9.9-km altitudes. A sharp increase in the downdraft mass flux at 9.9 km is seen between 1200 and 1400 UTC 6 July, <6 h prior to the onset of RI. Figure 20b shows the anomaly of the azimuthally averaged temperature

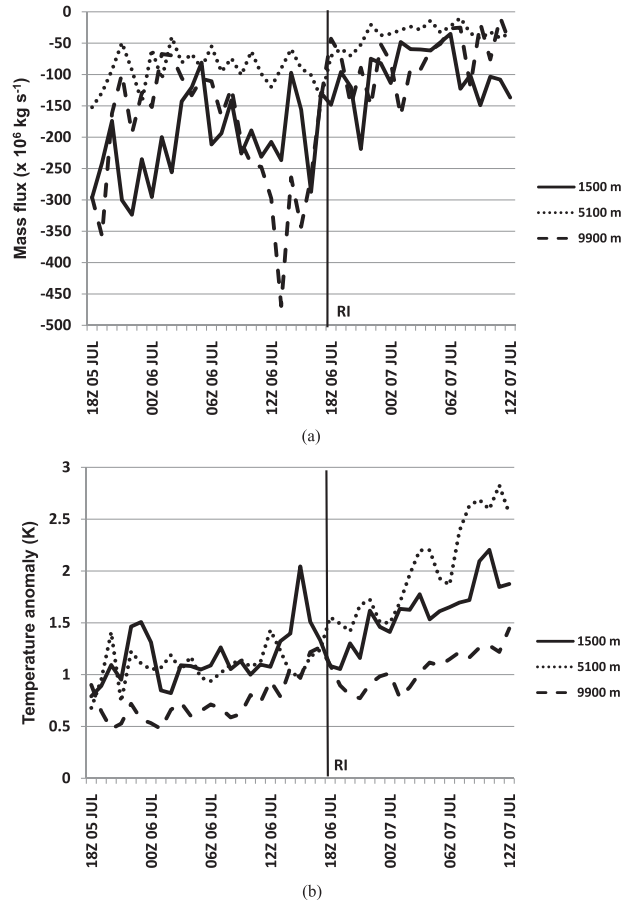FIG. 20. (a) Time series of inner-core downdraft mass flux for no-rain areas (10^6 kg s^{-1}). (b) Time series of anomaly (K) of the axisymmetric inner 30-km temperature from the total temperature. Black line denotes the onset of RI.

for radii <30 km compared with the azimuthally averaged temperature at all radii. A slow, steady increase in the temperature anomaly at all altitudes occurs prior to 1200 UTC 6 July. The impacts of the spike in downdraft mass flux from Fig. 20a are seen at 1600 UTC 6 July, when the 9.9-km temperature anomaly reaches 1.3 K before dropping back to <1 K. Once RI begins, the temperature anomalies at all three altitudes increase significantly, by 50%–100%. This evolution of the downdraft mass flux and temperature anomaly in the eye suggests the Shapiro and Willoughby (1982) and Heymsfield et al. (2001) mechanism may be operating here.

5. Discussion and concluding remarks

The 1.67-km MM5 simulation of Hurricane Dennis shown here reproduced the track, intensity, and precipitation evolution of Dennis reasonably well, including the

timing and intensification rate during RI. Large-scale and vortex-scale structures were in good agreement with analyses and observations. The primary and secondary circulation patterns steadily intensified during the simulation and the azimuthally averaged vorticity developed characteristics that were consistent with those of intensifying TCs seen in past observational studies.

For the convective-scale structure and evolution of Dennis, the following results were noted:

- Inner-core precipitation evolves from a mixture of convective and stratiform prior to RI to predominantly convective after RI has begun. The increase in convective precipitation coverage begins 3–6 h prior to the onset of RI.
- The mean inner-core vertical velocity in the convective regions is maximized in the 2–4-km layer prior to RI and extends over a much deeper layer after RI. No clear trend in mean convective updraft intensity is evident. The mean inner-core vertical velocity in the stratiform regions shows the typical pattern of 10–12-km updraft and 3–4-km downdraft peaks. Stratiform updraft intensity varies prior to RI and steadily increases after RI, though the magnitude is much weaker than in the convective regions. Stratiform downdrafts do not show a clear trend over time.
- Profiles of divergence in the convective and stratiform regions show low-level convergence and upper-level divergence in the convective regions, and low-level divergence, midlevel convergence, and upper-level divergence in the stratiform regions. Little time evolution occurs in the convective regions, while the strength of the low-level stratiform divergence and the depth of the midlevel stratiform convergence increase once RI has begun.
- Profiles of PV show maxima in the lower troposphere that intensify in the 6–12 h prior to RI for the convective regions. Once RI has begun, a clear maximum occurs in the middle levels consistent with the deepening of the mean updrafts and the increased height of the peak upper-level divergence. In the stratiform region PV is maximized in the midlevels throughout the time period, with increasing lower-troposphere PV in the 6 h prior to RI onset.
- Convective bursts occur throughout the simulation, with concentrations of bursts in three separate time periods. No clear relationship between the number of bursts and RI is evident. Significant variability in the proximity of bursts to the storm center occurs, sometimes reaching as much as 30-km variation from hour to hour.
- Clear differences exist between vertical velocity and reflectivity distributions for times with and without

a burst, but little difference is seen between burst times prior to and after RI.
- The strongest updrafts are associated with the highest potential vorticity.
- The total net vertical mass flux is maximized in the lowest 2 km. The most rapid increase in low-level net vertical mass flux occurs 3–6 h prior to RI.
- Areal coverage for weak, moderate, and strong updrafts is highly variable, but areal coverage of weak updrafts is most directly linked with RI. No relationship with the strongest updrafts is apparent.
- The bulk of the updraft and downdraft mass fluxes is accomplished by weak/moderate drafts. The time variation of the updraft mass flux for these draft magnitudes is closely linked with the intensity evolution, especially at low levels.
- The proportion of midlevel updraft mass flux accomplished by moderate/strong drafts (≥ 5 m s^{-1}) varies between 0% and 45%, with peaks coinciding with burst times. There is a peak in updraft mass flux contribution 6–12 h prior to RI, followed by a low-level vertical mass flux increase by the weak/moderate drafts and, subsequently, RI.
- Upper-level downdraft mass flux in rain-free areas shows a transient peak 6 h prior to RI. This peak in mass flux is followed by a peak in the eye temperature anomaly.

The onset of RI in this simulation is tied to an increase in the convective precipitation in the inner core. Stratiform precipitation does not play a significant role in the onset of RI; rather it responds to the vortex intensification through stronger updrafts in the mean. RI is also not tied to a dramatic increase in the number of bursts nor in the characteristics of the bursts, such as burst intensity. RI did begin 6–12 h after the occurrence of bursts between 0600 and 1200 UTC 6 July, which suggests a relationship exists between these bursts and RI.

Since no clear differences in burst structures and intensities were seen before and during RI, changes in the vortex structure must be a key factor explaining why RI occurred after the bursts from 0600 to 1200 UTC 6 July. The immediate precursor to RI in this case was the significant increase in updraft mass flux at 1.5-km altitude transported by updrafts in the weak/moderate (1–2 m s^{-1}) range at that altitude. Since the azimuthally averaged vertical velocity at this level ranges between 0.4 and 0.6 m s^{-1} (cf. Fig. 6), these updrafts likely include a significant contribution from the background secondary circulation, a feature that is driven by the radial gradient of buoyancy [i.e., "system buoyancy" as in Smith et al. (2005)]. However, locally buoyant bursts can accomplish a sizable proportion of the updraft mass flux, particularly

at midlevels, which is what has been emphasized by Malkus and Riehl (1960) and Simpson et al. (1998) and found in the modeling studies of Braun (2002) and AOF.

In the Dennis simulation, convective bursts occur intermittently throughout the entire period. These bursts result in an enhancement of the total updraft mass flux (Figs. 16 and 19) and an amplifying secondary circulation (Fig. 7), which in turn amplifies the primary circulation and inertial stability (Ooyama 1982; Schubert and Hack 1982). As the inertial stability increases, the efficiency with which diabatic heating is converted into the kinetic energy of the storm-scale primary circulation increases (e.g., Pendergrass and Willoughby 2009; Schubert and Vigh 2008; Nolan et al. 2007; Schubert and Hack 1982), and intensification results. The conversion efficiency is also enhanced by the location of the convective heating with respect to the radius of maximum winds. The two convective bursts at 1200 UTC 6 July were located an average of 40 km from the storm center, placing them within the RMW (cf. Fig. 6a). That fact, coupled with the general increase in inner-core convective precipitation between 1200 and 1800 UTC 6 July (cf. Fig. 10), led to a greater response in the temperature tendency that is manifested as an increased conversion efficiency to the primary circulation (Schubert and Vigh 2008). The increasing inertial stability associated with the intensifying vortex, seen in the increase in lower-tropospheric PV in both the convective and stratiform regions, and the more favorable placement of convective heating with respect to the RMW starting at 1200 UTC 6 July, is why RI occurred at ~1800 UTC 6 July.

The increasing impacts of heating and updraft mass flux from transient bursts on the vortex's primary circulation, realized as the TC intensifies and its inertial stability increases, represents a positive feedback that conditions the vortex for more rapid intensification. Once a threshold value of inertial stability is reached, rapid intensification can proceed, given a continued population of convective bursts within the inner core. As is the case in the Dennis simulation, the rapid intensification is first manifested as an increase in the low-level updraft mass flux, accomplished primarily by the weak-to-moderate drafts. Significant increases in the updraft mass flux then occur at higher altitudes, with the bulk of the increase again being accomplished primarily by the weak-to-moderate drafts. This interaction between the convective bursts and the background secondary circulation described here indicates a synergistic relationship between these features, and it supports the findings of Eastin et al. (2005) that updrafts, driven by local buoyancy, and the axisymmetric secondary circulation, driven by system buoyancy, are both important in rapid intensification.

Another way in which the locally buoyant updrafts and the system-scale circulation interact synergistically is in the evolution of upper-level downdraft mass flux. Associated with the convective bursts 6 h prior to RI is a short period of enhanced upper-level downdraft mass flux. This flux is followed by an increase in the temperature anomaly within the developing eye. This sequence of events is consistent with Schubert and Vigh (2008), who describe a confinement of the temperature anomaly when diabatic heating occurs within the RMW. An increase in the radial temperature gradient results in enhanced system buoyancy and a stronger axisymmetric secondary circulation, consistent with the mechanisms postulated by Shapiro and Willoughby (1982) and Heymsfield et al. (2001).

From the perspective of forecasting RI, there are two primary challenges: 1) to identify the threshold value of the inertial stability necessary for the efficient conversion of diabatic heating in the convective bursts to the primary circulation and 2) to know whether (and when) convective bursts will occur within the inner core once this inertial stability threshold is exceeded. A calculation of the efficiency of the conversion of the diabatic heating to kinetic energy based on the axisymmetric tangential wind, similar to what was done in Nolan et al. (2007), was performed on the Dennis simulation to see if the efficiency underwent a significant jump or step function at the moment of RI (not shown). Rather than increasing as a step function, the efficiency steadily increased as the vortex intensified, including at the onset of RI. Further research is planned to identify the key characteristics needed to identify this threshold value of the inertial stability necessary for RI and to determine how it varies by storm properties. Research is also needed to identify the conditions that lead to the development of convective bursts. In all likelihood the first challenge, that is, identifying the threshold value of the inertial stability, will be more predictable than the second challenge, that is, predicting burst initiation.

It should be emphasized that this work focused on convective-scale processes and their interaction with the vortex through their impacts on the evolution of the inner-core vertical mass flux. Vortex-scale processes, such as vortex Rossby wave dynamics and mesovortex interactions, have not been considered, though they certainly can play an important role in governing intensity evolution. Turbulent- and microscale processes, such as surface enthalpy and momentum fluxes, lateral entrainment and detrainment, and hydrometeor production and conversion, are also significant factors to consider when studying intensity change. A complete evaluation of the factors important in intensity change and RI would by necessity study processes spanning all of these scales, as

well as the interactions across scales. Additionally, the use of higher-resolution runs ($\Delta x \leq 1$ km) would better resolve the updraft and downdraft spectra and enable a more robust evaluation of their statistical properties and impacts on the vortex evolution.

The results obtained here will be compared with observations that have been collected both in this case and in other cases. Airborne Doppler data collected in Dennis from both NOAA P-3 and National Aeronautics and Space Administration (NASA) ER-2 aircraft (Halverson et al. 2007) can be used to compare the vortex structure and evolution, convective burst statistics, and vertical mass flux evolution prior to and during the RI of Dennis. Similar airborne data have been collected in other cases and this analysis can be extended to them. Tropical Rainfall Measuring Mission (TRMM) Precipitation Radar data (Simpson et al. 1988) and Cloudsat data (Stephens et al. 2002) can be examined to determine possible differences in convective burst statistics, such as the reflectivity distributions in bursts for cases undergoing RI and those not undergoing RI, though sampling may be a issue, particularly for Cloudsat.

REFERENCES

Beven, J., cited 2008: Tropical cyclone report: Hurricane Dennis. [Available online at http://www.nhc.noaa.gov/ms-word/TCR-AL042005_Dennis.doc.]

Black, M. L., R. W. Burpee, and F. D. Marks Jr., 1996: Vertical motion characteristics of tropical cyclones determined with airborne Doppler radial velocities. *J. Atmos. Sci.,* **53,** 1887–1909.

Bosart, L. F., C. S. Velden, W. E. Bracken, J. Molinari, and P. G. Black, 2000: Environmental Influences on the rapid intensification of Hurricane Opal (1995) over the Gulf of Mexico. *Mon. Wea. Rev.,* **128,** 322–352.

Braun, S. A., 2002: A cloud-resolving simulation of Hurricane Bob (1991): Storm structure and eyewall buoyancy. *Mon. Wea. Rev.,* **130,** 1573–1592.

——, 2006: High-resolution simulation of Hurricane Bonnie (1998). Part II: Water budget. *J. Atmos. Sci.,* **63,** 43–64.

——, and W.-K. Tao, 2000: Sensitivity of high-resolution simulations of Hurricane Bob (1991) to planetary boundary layer parameterizations. *Mon. Wea. Rev.,* **128,** 3941–3961.

——, M. T. Montgomery, and Z. Pu, 2006: High-resolution simulation of Hurricane Bonnie (1998). Part I: The organization of eyewall vertical motion. *J. Atmos. Sci.,* **63,** 19–42.

Cangialosi, J., and S. S. Chen, 2004: A numerical study of the topographic effects on structure and rainfall in Hurricane Georges (1998). Preprints, *26th Conf. on Hurricanes and Tropical Meteorology,* Miami, FL, Amer. Meteor. Soc., 13D.4. [Available online at http://ams.confex.com/ams/pdfpapers/75775.pdf.]

Cecil, D. J., E. J. Zipser, and S. W. Nesbitt, 2002: Reflectivity, ice scattering, and lightning characteristics of hurricane eyewalls and rainbands. Part I: Quantitative description. *Mon. Wea. Rev.,* **130,** 769–784.

Chen, S. S., W. Zhao, J. E. Tenerelli, R. H. Evans, and V. Halliwell, 2001: Impact of the AVHRR sea surface temperature on atmospheric forcing in the Japan/East Sea. *Geophys. Res. Lett.,* **28,** 4539–4545.

Cram, T. A., J. Persing, M. T. Montgomery, and S. A. Braun, 2007: A Lagrangian trajectory view on transport and mixing processes between the eye, eyewall, and environment using a high-resolution simulation of Hurricane Bonnie (1998). *J. Atmos. Sci.,* **64,** 1835–1856.

Davis, C., and L. F. Bosart, 2002: Numerical simulations of the genesis of Hurricane Diana (1984). Part II: Sensitivity of track and intensity prediction. *Mon. Wea. Rev.,* **130,** 1100–1124.

DeMaria, M., M. Mainelli, L. K. Shay, J. A. Knaff, and J. Kaplan, 2005: Further Improvements to the Statistical Hurricane Intensity Prediction Scheme (SHIPS). *Wea. Forecasting,* **20,** 531–543.

Dudhia, J., 1989: Numerical study of convection observed during the Winter Monsoon Experiment using a mesoscale two-dimensional model. *J. Atmos. Sci.,* **46,** 3077–3107.

Dunion, J. P., and C. S. Velden, 2004: The impact of the Saharan air layer on Atlantic tropical cyclone activity. *Bull. Amer. Meteor. Soc.,* **85,** 353–365.

Eastin, M. D., W. M. Gray, and P. G. Black, 2005: Buoyancy of convective vertical motions in the inner core of intense hurricanes. Part I: General statistics. *Mon. Wea. Rev.,* **133,** 188–208.

Emanuel, K. A., 1986: An air–sea interaction theory for tropical cyclones. Part I: Steady-state maintenance. *J. Atmos. Sci.,* **43,** 585–605.

Fierro, A. O., L. M. Leslie, E. R. Mansell, and J. M. Straka, 2008: Numerical simulations of the electrification and microphysics of the weakly electrified 9 February 1993 TOGA COARE squall line: Comparisons with observations. *Mon. Wea. Rev.,* **136,** 364–379.

——, R. F. Rogers, F. D. Marks Jr., and D. Nolan, 2009: The impact of horizontal grid spacing on the microphysical and kinematic structures of strong tropical cyclones simulated with the WRF-ARW model. *Mon. Wea. Rev.,* **137,** 3717–3743.

——, ——, ——, and ——, 2010: Impact of horizontal grid spacing on simulated tropical cyclone microphysical and kinematic structure. *Mon. Wea. Rev.,* in press.

Gamache, J. F., and R. A. Houze Jr., 1982: Mesoscale air motions associated with a tropical squall line. *Mon. Wea. Rev.,* **110,** 118–135.

Gentry, R. C., T. T. Fujita, and R. C. Sheets, 1970: Aircraft, spacecraft, satellite and radar observations of Hurricane Gladys, 1968. *J. Appl. Meteor.,* **9,** 837–850.

Grell, G. A., J. Dudhia, and D. R. Stauffer, 1994: A description of the fifth generation Penn State/NCAR Mesoscale Model (MM5). NCAR Tech. Note NCAR/TN-398+STR, 138 pp.

Halverson, J., and Coauthors, 2007: NASA's Tropical Cloud Systems and Processes Experiment. *Bull. Amer. Meteor. Soc.,* **88,** 867–882.

Hendricks, E. A., M. T. Montgomery, and C. A. Davis, 2004: The role of "vortical" hot towers in the formation of Tropical Cyclone Diana (1984). *J. Atmos. Sci.,* **61,** 1209–1232.

Hennon, P. A., 2006: The role of the ocean in convective burst initiation: Implications for tropical cyclone intensification. Ph.D. dissertation, The Ohio State University, 185 pp.

Hertenstein, R. F., and W. H. Schubert, 1991: Potential vorticity anomalies associated with squall lines. *Mon. Wea. Rev.,* **119,** 1663–1672.

Heymsfield, G. M., J. B. Halverson, J. Simpson, L. Tian, and T. P. Bui, 2001: ER-2 Doppler radar investigations of the eyewall of Hurricane Bonnie during the Convection and Moisture Experiment-3. *J. Appl. Meteor.,* **40,** 1310–1330.

Hong, X., S. W. Chang, S. Raman, L. K. Shay, and R. Hodur, 2000: The Interaction between Hurricane Opal (1995) and a warm core ring in the Gulf of Mexico. *Mon. Wea. Rev.,* **128,** 1347–1365.

Houze, R. A., Jr., 1977: Structure and dynamics of a tropical squall–line system. *Mon. Wea. Rev.,* **105,** 1540–1567.

——, F. D. Marks Jr., and R. A. Black, 1992: Dual-aircraft investigation of the inner core of Hurricane Norbert. Part II: Mesoscale distribution of ice particles. *J. Atmos. Sci.,* **49,** 943–963.

Johnson, R. H., 1984: Partitioning tropical heat and moisture budgets into cumulus and mesoscale components: Implications for cumulus parameterization. *Mon. Wea. Rev.,* **112,** 1590–1601.

Jorgensen, D. P., E. J. Zipser, and M. A. LeMone, 1985: Vertical motions in intense hurricanes. *J. Atmos. Sci.,* **42,** 839–856.

Kain, J. S., and J. M. Fritsch, 1993: Convective parameterization for mesoscale models: The Kain–Fritsch scheme. *The Representation of Cumulus Convection in Numerical Models, Meteor. Monogr.,* No. 46, Amer. Meteor. Soc., 165–170.

Kaplan, J., and M. DeMaria, 2003: Large-scale characteristics of rapidly intensifying tropical cyclones in the North Atlantic basin. *Wea. Forecasting,* **18,** 1093–1108.

Karyampudi, V. M., G. S. Lai, and J. Manobianco, 1998: Impact of initial conditions, rainfall assimilation, and cumulus parameterization on simulations of Hurricane Florence (1988). *Mon. Wea. Rev.,* **126,** 3077–3101.

Kelley, O. A., J. Stout, and J. B. Halverson, 2004: Tall precipitation cells in tropical cyclone eyewalls are associated with tropical cyclone intensification. *Geophys. Res. Lett.,* **31,** L24112, doi:10.1029/2004GL021616.

Kilpatrick, K. A., G. P. Podestá, and R. Evans, 2001: Overview of the NOAA/NASA Advanced Very High Resolution Radiometer Pathfinder algorithm for sea surface temperature and associated matchup database. *J. Geophys. Res.,* **106** (C5), 9179–9197.

Kossin, J. P., and M. D. Eastin, 2001: Two distinct regimes in the kinematic and thermodynamic structure of the hurricane eye and eyewall. *J. Atmos. Sci.,* **58,** 1079–1090.

——, and W. H. Schubert, 2001: Mesovortices, polygonal flow patterns, and rapid pressure falls in hurricane-like vortices. *J. Atmos. Sci.,* **58,** 2196–2209.

Lin, Y.-L., R. D. Farley, and H. D. Orville, 1983: Bulk parameterization of the snow field in a cloud model. *J. Climate Appl. Meteor.,* **22,** 1065–1092.

Liu, Y.-L., D.-L. Zhang, and M. K. Yau, 1997: A multiscale numerical study of Hurricane Andrew (1992). Part I: Explicit simulation and verification. *Mon. Wea. Rev.,* **125,** 3073–3093.

——, ——, and ——, 1999: A multiscale numerical study of Hurricane Andrew (1992). Part II: Kinematics and inner-core structures. *Mon. Wea. Rev.,* **127,** 2597–2616.

Lord, S. J., H. E. Willoughby, and J. M. Piotrowicz, 1984: Role of a parameterized ice-phase microphysics in an axisymmetric, nonhydrostatic tropical cyclone model. *J. Atmos. Sci.,* **41,** 2836–2848.

Malkus, J. S., and H. Riehl, 1960: On the dynamics and energy transformations in steady state hurricanes. *Tellus,* **12,** 1–20.

Mapes, B. E., and R. A. Houze Jr., 1995: Diabatic divergence profiles in western Pacific mesoscale convective systems. *J. Atmos. Sci.,* **52,** 1807–1828.

Marks, F. D., 1985: Evolution of the structure of precipitation in Hurricane Allen (1980). *Mon. Wea. Rev.,* **113,** 909–930.

——, and R. A. Houze Jr., 1987: Inner core structure of Hurricane Alicia from airborne Doppler radar observations. *J. Atmos. Sci.,* **44,** 1296–1317.

——, and L. K. Shay, 1998: Landfalling tropical cyclones: Forecast problems and associated research opportunities. *Bull. Amer. Meteor. Soc.,* **79,** 305–323.

May, P. T., and D. K. Rajopadhyaya, 1996: Wind profiler observations of vertical motion and precipitation microphysics of a tropical squall line. *Mon. Wea. Rev.,* **124,** 621–633.

McFarquhar, G. M., H. Zhang, G. Heymsfield, R. Hood, J. Dudhia, J. B. Halverson, and F. Marks, 2006: Factors affecting the evolution of Hurricane Erin (2001) and the distributions of hydrometeors: role of microphysical processes. *J. Atmos. Sci.,* **63,** 127–150.

Molinari, J., S. Skubis, and D. Vollaro, 1995: External influences on hurricane intensity. Part III: Potential vorticity structure. *J. Atmos. Sci.,* **52,** 3593–3606.

Montgomery, M. T., and R. J. Kallenbach, 1997: A theory for vortex Rossby waves and its application to spiral bands and intensity changes in hurricanes. *Quart. J. Roy. Meteor. Soc.,* **123,** 435–465.

——, V. A. Vladimirov, and P. V. Denissenko, 2002: An experimental study on hurricane mesovortices. *J. Fluid Mech.,* **471,** 1–32.

——, M. E. Nicholls, T. A. Cram, and A. B. Saunders, 2006: A vortical hot tower route to tropical cyclogenesis. *J. Atmos. Sci.,* **63,** 355–386.

Nolan, D. S., 2007: What is the trigger for tropical cyclogenesis? *Aust. Meteor. Mag.,* **56,** 241–266.

——, and L. D. Grasso, 2003: Nonhydrostatic, three-dimensional perturbations to balanced, hurricane-like vortices. Part II: Symmetric response and nonlinear simulations. *J. Atmos. Sci.,* **60,** 2717–2745.

——, Y. Moon, and D. P. Stern, 2007: Tropical cyclone intensification from asymmetric convection: energetics and efficiency. *J. Atmos. Sci.,* **64,** 3377–3405.

Ooyama, K., 1969: Numerical simulation of the life cycle of tropical cyclones. *J. Atmos. Sci.,* **26,** 3–40.

——, 1982: Conceptual evolution of the theory and modeling of the tropical cyclone. *J. Meteor. Soc. Japan,* **60,** 369–380.

Pendergrass, A. G., and H. E. Willoughby, 2009: Diabatically induced secondary flows in tropical cyclones. Part I: Quasi-steady forcing. *Mon. Wea. Rev.,* **137,** 805–821.

Persing, J., and M. T. Montgomery, 2003: Hurricane superintensity. *J. Atmos. Sci.,* **60,** 2349–2371.

Reasor, P. D., M. Eastin, and J. F. Gamache, 2009: Rapidly intensifying Hurricane Guillermo (1997). Part I: Low-wavenumber structure and evolution. *Mon. Wea. Rev.,* **137,** 603–631.

Rodgers, E. B., W. S. Olson, V. M. Karyampudi, and H. F. Pierce, 1998: Satellite-derived latent heating distribution and environmental

influences in Hurricane Opal (1995). *Mon. Wea. Rev.,* **126,** 1229–1247.

Rogers, R. F., S. Chen, J. Tenerelli, and H. Willoughby, 2003: A numerical study of the impact of vertical shear on the distribution of rainfall in Hurricane Bonnie (1998). *Mon. Wea. Rev.,* **131,** 1577–1599.

——, and Coauthors, 2006: The Intensity Forecasting Experiment: A NOAA multiyear field program for improving tropical cyclone intensity forecasts. *Bull. Amer. Meteor. Soc.,* **87,** 1523–1537.

——, M. L. Black, S. S. Chen, and R. A. Black, 2007: An evaluation of microphysics fields from mesoscale model simulations of tropical cyclones. Part I: Comparisons with observations. *J. Atmos. Sci.,* **64,** 1811–1834.

Rotunno, R., and K. A. Emanuel, 1987: An air–sea interaction theory for tropical cyclones. Part II: Evolutionary study using a nonhydrostatic axisymmetric numerical model. *J. Atmos. Sci.,* **44,** 542–561.

Schubert, W. H., and J. J. Hack, 1982: Inertial stability and tropical cyclone development. *J. Atmos. Sci.,* **39,** 1687–1697.

——, and J. S. Vigh, 2008: Rapid development of the tropical cyclone warm core. Preprints, *28th Conf. on Hurricanes and Tropical Meteorology,* Orlando, FL, Amer. Meteor. Soc., 14C.3. [Available online at http://ams.confex.com/ams/pdfpapers/138263.pdf.]

——, M. T. Montgomery, R. K. Taft, T. A. Guinn, S. R. Fulton, J. P. Kossin, and J. P. Edwards, 1999: Polygonal eyewalls, asymmetric eye contraction, and potential vorticity mixing in hurricanes. *J. Atmos. Sci.,* **56,** 1197–1223.

Shapiro, L. J., and H. E. Willoughby, 1982: The response of balanced hurricanes to local sources of heat and momentum. *J. Atmos. Sci.,* **39,** 378–394.

Shay, L. K., G. J. Goni, and P. G. Black, 2000: Effects of a warm oceanic feature on Hurricane Opal. *Mon. Wea. Rev.,* **128,** 1366–1383.

Simpson, J., R. F. Adler, and G. R. North, 1988: A proposed Tropical Rainfall Measuring Mission (TRMM) satellite. *Bull. Amer. Meteor. Soc.,* **69,** 278–295.

——, J. B. Halverson, B. S. Ferrier, W. A. Petersen, R. H. Simpson, R. Blakeslee, and S. L. Durden, 1998: On the role of "hot towers" in tropical cyclone formation. *Meteor. Atmos. Phys.,* **67,** 15–35.

Smagorinsky, J., S. Manabe, and J. L. Holloway Jr., 1965: Numerical results from a nine-level general circulation model of the atmosphere. *Mon. Wea. Rev.,* **93,** 727–768.

Smith, R. K., M. T. Montgomery, and H. Zhu, 2005: Buoyancy in tropical cyclones and other rapidly rotating atmospheric vortices. *Dyn. Atmos. Oceans,* **40,** 189–208.

Squires, K., and S. Businger, 2008: The morphology of eyewall lightning outbreaks in two category 5 hurricanes. *Mon. Wea. Rev.,* **136,** 1706–1726.

Stauffer, D. R., and N. L. Seaman, 1990: Use of four-dimensional data assimilation in a limited-area mesoscale model. Part I: Experiments with synoptic-scale data. *Mon. Wea. Rev.,* **118,** 1250–1277.

Steiner, M., R. A. Houze, and S. E. Yuter, 1995: Climatological characterization of three-dimensional storm structure from operational radar and rain gauge data. *J. Appl. Meteor.,* **34,** 1978–2007.

Stephens, G. L., and Coauthors, 2002: The Cloudsat mission and the A-Train. *Bull. Amer. Meteor. Soc.,* **83,** 1771–1790.

Stern, D. P., and D. S. Nolan, 2009: Reexamining the vertical structure of tangential winds in tropical cyclones: Observations and theory. *J. Atmos. Sci.,* **66,** 3579–3600.

Tao, W. K., and J. Simpson, 1989: Modeling study of a tropical squall-type convective line. *J. Atmos. Sci.,* **46,** 177–202.

Tenerelli, J. E., and S. S. Chen, 2002: Intensity change and eyewall replacement in Hurricane Floyd (1999). Preprints, *25th Conf. on Hurricanes and Tropical Meteorology,* San Diego, CA, Amer. Meteor. Soc., 3C.2. [Available online at http://ams.confex.com/ams/pdfpapers/38005.pdf.]

——, and ——, 2004: Influence of initial vortex structure on the simulation of hurricane lifecycles. Preprints, *26th Conf. on Hurricanes and Tropical Meteorology,* Miami, FL, Amer. Meteor. Soc., 15C.3. [Available online at http://ams.confex.com/ams/pdfpapers/75958.pdf.]

Tory, K. J., M. T. Montgomery, and N. E. Davidson, 2006: Prediction and diagnosis of tropical cyclone formation in an NWP system. Part I: The critical role of vortex enhancement in deep convection. *J. Atmos. Sci.,* **63,** 3077–3090.

Yuter, S. E., and R. A. Houze Jr., 1995: Three-dimensional kinematic and microphysical evolution of Florida cumulonimbus. Part III: Vertical mass transport, mass divergence, and synthesis. *Mon. Wea. Rev.,* **123,** 1964–1983.

Zhang, D.-L., and R. A. Anthes, 1982: A high-resolution model of the planetary boundary layer—Sensitivity tests and comparisons with SESAME-79 data. *J. Appl. Meteor.,* **21,** 1594–1609.

Zipser, E. J., 1977: Mesoscale and convective–scale downdrafts as distinct components of squall-line structure. *Mon. Wea. Rev.,* **105,** 1568–1589.

——, 2003: Some views on "hot towers" after 50 years of tropical field programs and two years of TRMM data. *Cloud Systems, Hurricanes, and the Tropical Rainfall Measuring Mission (TRMM): A Tribute to Dr. Joanne Simpson, Meteor. Monogr.,* No. 51, Amer. Meteor. Soc., 49–58.